Robust population inversion in three-level systems by composite pulses

Cheng Zhang,[1,2] Yang Liu,[1,2] Zhi-Cheng Shi,[1,2,*] Jie Song,[3] Yan Xia,[1,2,†] and Shi-Biao Zheng[1,2]

[1] *Fujian Key Laboratory of Quantum Information and Quantum Optics (Fuzhou University), Fuzhou 350108, China*
[2] *Department of Physics, Fuzhou University, Fuzhou 350108, China*
[3] *Department of Physics, Harbin Institute of Technology, Harbin 150001, China*

(Dated: April 11, 2022)

In this work, we exploit the idea of composite pulses to achieve robust population inversion in a three-level quantum system. The scheme is based on the modulation of the coupling strength, while the other physical parameters remain unchanged. The composite pulses sequence is designed by vanishing high-order error terms, and can compensate the systematic errors to any desired order. In particular, this scheme keeps a good performance under the disturbance of waveform deformations. This trait ensures that population inversion can be nearly obtained even when the pulse sequence has a short jump delay. As an example, we employ the designed composite pulse sequence to prepare the W state in a robust manner in the superconducting circuits. The numerical results show that the fidelity can still maintain a high level in a decoherence environment.

I. INTRODUCTION

Robust control of quantum states is one of the crucial topics in quantum information processing (QIP) [1–8]. Through controlling the external fields, the initial state of a quantum system can be driven into the desired target state. During this process, many requirements need to be satisfied. The first one is to quickly accomplish quantum operations, because the coherence time of quantum systems is generally very short. Once the operation time is sufficiently long, the advantages of quantum computation would gradually be lost. The second one is to perform quantum operations in a robust way. As is well known, the infidelity of quantum logic gates needs to be below the fault-tolerant threshold (10^{-4}) to protect the reliability of quantum computation [9]. However, quantum systems always suffer from the harmful effect of external noises, which may be caused by the imperfect knowledge of quantum systems or the fluctuations of external fields, etc. These external noises finally lead to a sharp decline in the fidelity of quantum gates. In response, quantum control theory is developed to tackle these problems.

Quantum control theory has been successfully applied in single [10, 11] and multibody systems [12, 13]. At the same time, this theory has made new progress in quantum state preparations [14–20], quantum gate operations [21–32], and quantum error corrections [33–38]. During the quantum control process, the primary mission is to design an appropriate pulse shape of the control fields to drive the system evolution as we expect. The traditional method is to employ the adiabatic passage (AP) [39–45], which matches the initial (target) state to one instantaneous eigenstate as an evolution path of the system. The AP requests that the physical parameters must vary slowly enough so as to meet the adiabatic condition. It is widely known that there are two relevant well-established techniques: the chirped rapid adiabatic passage (CHIRAP) [40–43] and the stimulated Raman adiabatic passage (STIRAP) [46–48]. The former proposes to apply a chirped pulse to modulate the frequency detuning of the system. The slow chirp rate ensures that the adiabatic condition is strictly satisfied. Therefore, one can drive the system evolution along a given eigenstate and suppress transitions to other eigenstates [42]. The latter is one of the most popular methods for quantum control in three-level systems and has since been widely expanded to other fields [49]. In the STIRAP, the Stokes pulse and the pump pulse are applied in a counterintuitive order, and one can achieve a successful population transfer between two states under the two-photon resonance condition in three-level systems [49]. The main feature of AP is that the robustness against parameter fluctuations could be achieved at the expense of operation speed and accuracy. However, once the adiabatic condition cannot be satisfied well, the accuracy would be sharply dropped due to the imperfect adiabatic path.

To optimize the speed and accuracy of AP, an improved and acclaimed technique named shortcut to adiabaticity (STA) [50–52] has been developed. There are two common methods in the STA technique: Lewis-Riesenfeld invariants [53] and transitionless quantum driving [54–56]. The main idea of STA is to design the pulse shape to canceling nonadiabatic transitions through an additional Hamiltonian. Nevertheless, it depends heavily on the precisely known physical parameters, and strong fluctuations of parameters might make this method inefficient. Recently, optimal control (OP) has become another popular way to achieve high-fidelity quantum operations [12, 57–64]. One disadvantage of OP is that the pulse shape is always intricate and nonanalytic because it is achieved by using advanced mathematical algorithms. As a result, the design process only yields certain numerical solutions. In order to take account of the robustness and accuracy of quantum control, one can turn to the composite pulses

* szc2014@yeah.net
† xia-208@163.com

(CPs) technique, where the physical parameters are flexible to design and the shapes are readily implemented in experiments due to its commonality.

The CPs technique was born in the field of nuclear magnetic resonance [65–68]. Over the past decade, CPs have provided a lot of solutions in quantum computation [69–75] due to their extremely high accuracy, robustness against errors, and extraordinary flexibility [76]. Generally speaking, the CPs technique is composed of a series of precise constant pulses with different relative phases. These pulses are usually imposed on external laser fields, electric fields, magnetic fields, or radio-frequency fields, etc. It is shown that the phase-modulated composite pulses (PMCPs) can not only improve the robustness against errors (broadband pulse), but also enhance the sensitivity and selectivity of excitation (narrowband pulse) [77]. Recently, the PMCPs have also been designed to produce a rotation in the Bloch sphere [71], where the errors resulting from the pulse area are gradually compensated with the increase of the pulse number. Another application of PMCPs is to implement the NOT gate, and this scheme is robust against both offset uncertainties and control field variations by a very small number of modulation parameters [75].

However, when the system phase cannot be modulated or the system does not carry phase information, PMCPs would be invalid. In order to supplement the deficiency of composite pulses, researchers turn their attention to some other adjustable parameters. Therefore, the detuning-modulated composite pulses (DMCPs) and the strength-modulated composite pulses (SMCPs) have become two additional promising methods. Recently, based on photonic integrated circuits, Greener *et al.* applied DMCPs in the coupled optical waveguide model to achieve complete light transfer [78]. SMCPs are used to implement dynamically corrected single-qubit gates on singlet-triplet qubits [79, 80], where qubit manipulations are handled by adjusting the electrically controlled exchange coupling strength. Note that most works [69–80] of CPs are based on two-level systems. Recently, the CPs have been extended to the three-level systems and have provided many creative works [81–87], such as the implementation of high-fidelity composite quantum gates [81, 82] and the efficient detection of chiral molecules [83]. It is worth mentioning that those works [81–83] still focus on the phase modulation in three-level systems.

In this paper, based on the composite pulses technique, we develop a general SMCPs scheme for robust population inversion in three-level systems. According to the Taylor expansion, the final transition probability expression is rearranged into a series of error terms. With predetermined phases and pulse area, these error terms could be effectively eliminated from low order to high order by properly adjusting coupling strengths. In addition, we investigate the influence of waveform deformation on the transition probability. The results show that slight deformation still allows the SMCPs to work well, except for the heavily deformed case. In the end, we further apply the current SMCPs scheme to prepare the W state in the superconducting quantum interference device (SQUID) model, and the numerical simulations demonstrate that the SMCPs can still maintain a robust performance in a decoherence environment.

The structure of this paper is organized as follows. In Sec. II, we present the design procedure of the SMCPs in the three-level system, which are directly derived from the total composite propagator. In Sec. III, we illustrate how to eliminate the effect of pulse area error by SMCPs with the specific number of pulses. Here, the sequence of up to seven pulses has been studied, and the longer sequence could also be obtained in a similar way. Then, we analyze the impact of the waveform deformation of CPs on the performance of the transition probability and compare our scheme with other composite pulses. In Sec. IV, we give the application of the SMCPs scheme in robustly preparing the W state in the superconducting circuits. Finally, we give the conclusion in Sec. V.

II. THEORETICAL MODEL

In this section, we elaborate on the design procedure of the general pulse waveform in a three-level system with Λ-type structure. This system has been regarded as a paradigmatic model in many branches of physics, including atomic and molecular [88–90], quantum information science [91], and some other fields [92–95]. The basic structure is shown in Fig. 1, where $|g\rangle$ and $|f\rangle$ are two ground states and $|e\rangle$ is the excited state. There are two control fields that drive two transitions: $|g\rangle \leftrightarrow |e\rangle$ and $|f\rangle \leftrightarrow |e\rangle$. Meanwhile, the transition frequency of the three-level system and the carrier frequency of the control fields satisfy the two-photon resonance condition [96]. Note that the direct transition between two ground states

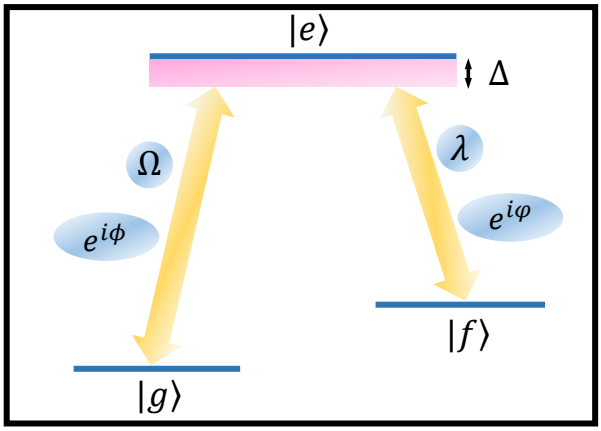

FIG. 1. A Λ-type three-level system driven by two control fields in the two-photon resonance regime.

is forbidden. In the interaction picture, the dynamics of the system can be described by the following Hamiltonian ($\hbar = 1$ hereafter):

$$H = \Delta|e\rangle\langle e| + \frac{1}{2}\Big(\Omega e^{i\phi}|g\rangle\langle e| + \lambda e^{i\varphi}|f\rangle\langle e| + \text{H.c.}\Big), \quad (1)$$

where Ω and ϕ (λ and φ) are the coupling strength and the phase of the transition $|g\rangle \leftrightarrow |e\rangle$ ($|f\rangle \leftrightarrow |e\rangle$), and Δ is the single-photon detuning. When the detuning is much larger than two coupling strengths (i.e., $|\Delta| \gg \Omega, \lambda$), the excited state $|e\rangle$ could be adiabatically eliminated [97]. Then, the three-level system would be reduced as an effective two-level system. In the following, we study the system dynamics including the excited state, and thus do not focus on this situation.

The propagator U of this three-level system satisfies the following Schrödinger equation:

$$i\dot{U} = HU. \quad (2)$$

When the Hamiltonian given by Eq. (1) is time independent, the solution of this equation becomes $U = \exp(-iHT)$, where T is the time duration. It is instructive to adopt its matrix form in the basis $\{|g\rangle, |f\rangle, |e\rangle\}$, which reads:

$$U(\Theta) = \begin{bmatrix} U_{11} & U_{12} & U_{13} \\ U_{21} & U_{22} & U_{23} \\ U_{31} & U_{32} & U_{33} \end{bmatrix}, \quad (3)$$

where

$$U_{11} = \cos^2\Theta + e^{-i\delta}(\cos\frac{A}{2} + \frac{i\Delta}{\sqrt{1+\Delta^2}}\sin\frac{A}{2})\sin^2\Theta,$$

$$U_{22} = \sin^2\Theta + e^{-i\delta}(\cos\frac{A}{2} + \frac{i\Delta}{\sqrt{1+\Delta^2}}\sin\frac{A}{2})\cos^2\Theta,$$

$$U_{33} = e^{-i\delta}(\cos\frac{A}{2} - \frac{i\Delta}{\sqrt{1+\Delta^2}}\sin\frac{A}{2}),$$

$$U_{12} = \frac{1}{2}e^{-i\delta}e^{i\Psi}(\cos\frac{A}{2} + \frac{i\Delta}{\sqrt{1+\Delta^2}}\sin\frac{A}{2} - e^{i\delta})\sin 2\Theta,$$

$$U_{21} = \frac{1}{2}e^{-i\delta}e^{-i\Psi}(\cos\frac{A}{2} + \frac{i\Delta}{\sqrt{1+\Delta^2}}\sin\frac{A}{2} - e^{i\delta})\sin 2\Theta,$$

$$U_{13} = -e^{-i2\delta}U_{31}^* = -ie^{-i\delta}e^{i\phi}\frac{\sin\Theta}{\sqrt{1+\Delta^2}}\sin\frac{A}{2},$$

$$U_{23} = -e^{-i2\delta}U_{32}^* = -ie^{-i\delta}e^{i\varphi}\frac{\cos\Theta}{\sqrt{1+\Delta^2}}\sin\frac{A}{2}.$$

Here, $\Theta = \arctan(\Omega/\lambda)$, $\delta = \int_0^T \Delta/2\ dt$, the phase difference $\Psi = \phi - \varphi$, and the expression of the total pulse area A is

$$A = \int_0^T \sqrt{\Omega^2 + \lambda^2 + \Delta^2}\ dt. \quad (4)$$

Obviously, when the pulse area $A = 2\pi$, two ground states are decoupled from the excited state $|e\rangle$ so that we can only concentrate on the subspace $\{|g\rangle, |f\rangle\}$. Then, when the system is initially in the ground state $|g\rangle$, the transition probability P of the target state $|f\rangle$ becomes

$$P = |U_{21}|^2 = \cos^2\left(\frac{\pi\Delta}{2\sqrt{1+\Delta^2}}\right)\sin^2 2\Theta. \quad (5)$$

It is easily found from Eq. (5) that the detuning Δ is required to be zero in order to achieve complete population inversion for the single pulse.

Then, one can see from Eq. (4) that two kinds of uncertainties would cause the pulse area error when $\Delta = 0$. The first one is the coupling strength error, which may be caused by the inhomogeneity of the control fields. Another one is the inaccurate pulse duration, which may be limited to the experiment condition or manual operation accuracy. Note that tiny errors in the pulse area would have a significant effect on population inversion. This can be demonstrated as follows. Suppose that the pulse area error is represented by ϵ, and a deviation in the original pulse area reads $A = A(1+\epsilon)$. As a result, the transition probability given by Eq. (5) is rewritten as

$$P(\epsilon) = \sin^4\frac{A(1+\epsilon)}{4}\sin^2 2\Theta. \quad (6)$$

In order to study how the pulse area error makes an impact on population inversion, the transition probability $P(\epsilon)$ given by Eq. (6) is expanded as the Taylor series,

$$P(\epsilon) = \alpha_0 + \alpha_1\epsilon + \alpha_2\epsilon^2 + O(\epsilon^3), \quad (7)$$

where α_j is the jth-order coefficient, $j = 0, 1, 2, \cdots$. Actually, α_0 is the transition probability in the absence of the pulse area error. By setting the pulse area $A = 2\pi(1+\epsilon)$, the first three order coefficients are

$$\alpha_0 = \sin^2 2\Theta,\ \alpha_1 = 0,\ \alpha_2 = -\frac{1}{2}\pi^2\sin^2 2\Theta. \quad (8)$$

Notice that the first-order coefficient α_1 is automatically eliminated because all odd-order coefficients contain the term $\sin(A/2)$. Here, $\Theta = \pi/4 + k\pi/2$ is the indispensable condition to achieve population inversion, i.e., $\alpha_0 = 1$. We can observe from Eq. (8) that the second-order coefficient α_2 has the same monotony with α_0 because they have the same term $\sin^2 2\Theta$. This means that the error would also reach maximum if we achieve complete population inversion. In Figs. 2(a) and 2(b), the red solid curve represents $P(\epsilon)$ as a function of the pulse area error ϵ, which shows that the transition probability sharply drops near $\epsilon = 0$. Hence, the single-pulse scheme does not possess a robust manner against the pulse area error.

In order to solve this problem, next we put forward the SMCPs scheme. The sequence is composed of multiple single pulses, where only coupling strengths for each pulse are different. For the compact expression, we label the Hamiltonian and the propagator of the nth pulse as H_n

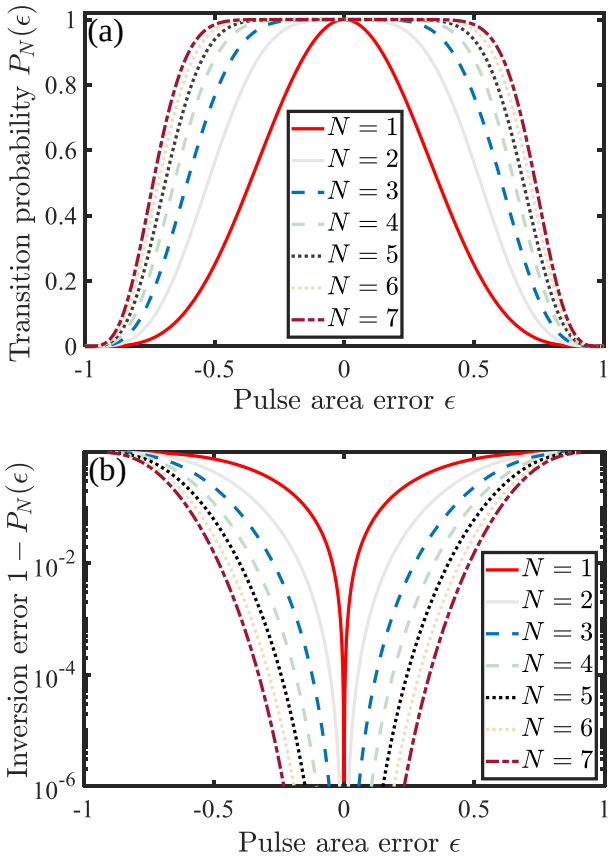

FIG. 2. (a) Transition probability $P_N(\epsilon)$ vs the pulse area error ϵ under different pulses sequences. (b) Inversion error $1-P_N(\epsilon)$ vs the pulse area error ϵ. All Θ_n come from Table I.

and $U_n(\Theta_n)$, respectively. Then, the general form of the total propagator for the N-pulses sequence can be written as

$$U^{(N)}=U_N(\Theta_N)U_{N-1}(\Theta_{N-1})\cdots U_2(\Theta_2)U_1(\Theta_1). \quad (9)$$

The detailed derivation of the total propagator $U^{(N)}$ without the pulse area error is presented in Appendix A. Note that the transition probability of every state is associated with both the detuning and the coupling strengths of each pulse. For simplicity, we assume each pulse is in the resonant regime ($\Delta_n = 0$) in the following.

The target of this work is to achieve robust population inversion by SMCPs. Without loss of generality, we assume the initial state is $|\psi_i\rangle = |g\rangle$; then the target state becomes $|\psi_f\rangle = |f\rangle$. Each pulse area is represented as $2\pi(1+\epsilon)$, and we label $P_N(\epsilon)$ as the transition probability of the state $|f\rangle$ in the N pulses sequence. Similar to the derivations in Eq. (7), $P_N(\epsilon)$ can be written in the following form by the Taylor expansion:

$$P_N(\epsilon) = \alpha_{N,0} + \alpha_{N,1}\epsilon + \alpha_{N,2}\epsilon^2 + \cdots + O(\epsilon^n), \quad (10)$$

where $\alpha_{N,j}$ is the jth-order coefficient in the N pulses sequence, and its expression can be deduced from the total propagator given by Eq. (9).

Here, we do not intend to change the pulse area and phases of this system, and thus the pulse area and phases are predetermined by constants during the evolution process. Note that all odd-order coefficients $\alpha_{N,j}(j = 2n-1)$ would vanish if the pulse area of each pulse is equal to 2π, i.e., $A_1 = \cdots = A_N = 2\pi$. As a result, only even-order coefficients are left in Eq. (10). By modulating the parameters Θ_n $(n = 1,\ldots,N)$, we demand that the zeroth-order coefficient be unity, which ensures complete population inversion, and other even-order coefficients vanish as many as possible. Note that according to the expression $\Theta_n = \arctan(\Omega_n/\lambda_n)$, we can keep the coupling strength λ_n unchanged and alter the coupling strength Ω_n to implement the modulation of Θ_n. This means that we only adjust one of the coupling strengths to achieve robust population inversion in the three-level system.

To be specific, if the sequence is composed of N pulses, we first solve N equations to obtain the solutions of Θ_n, i.e.,

$$\begin{cases} \alpha_{N,0} = 1, \\ \alpha_{N,2} = 0, \\ \quad \cdots \\ \alpha_{N,2N-2} = 0. \end{cases} \quad (11)$$

Then, we calculate different coupling strengths Ω_n of each pulse according to the expression $\Omega_n = \lambda_n \tan\Theta_n$. Consequently, we have the composite pulses sequence to achieve population inversion. In this situation, the transition probability is accurate to the order of $O(\epsilon^{2N-2})$. Compared with the single-pulse scheme, the transition probability in the SMCPs scheme has a better robust manner against the pulse area error ϵ since the high-order coefficients disappear. In other words, eliminating more high-order coefficients in Eq. (10) could further suppress the detrimental effect of the pulse area error. When the composite pulses sequence is sufficiently short, the analytical results are readily obtained by solving the corresponding equations. However, the long pulse sequence would increase the number of equations. As a result, it is difficult to derive the analytical results. Instead, we provide the numerical solutions for the long pulse sequence. In order to demonstrate this issue in more detail, we exemplify the SMCPs scheme with a specific number of pulses below.

III. STRENGTH-MODULATED COMPOSITE PULSES SCHEME

In this section, we study how to design the SMCPs to achieve robust population inversion when the pulse area and phases remain unchanged. For simplicity, we uniformly set $A_n = 2\pi$, $\phi_n = \pi/2$, $\varphi_n = 0$, and assume the system always works in the resonance regime (i.e., $\Delta_n = 0$). Note that Θ_n are only the adjustable parameters.

A. Two pulses

The propagator in the two-pulses sequence can be expressed by

$$U^{(2)} = U_2(\Theta_2)U_1(\Theta_1). \tag{12}$$

According to the propagator $U^{(2)}$ given by Eq. (12), the transition probability $P_2(\epsilon)$ of the state $|f\rangle$ is

$$P_2(\epsilon) = \frac{1}{4}\Big\{ \sin^2\pi\epsilon\big[\cos\Theta_1\sin\Theta_2+\cos\Theta_2(2\sin\Theta_1+\sin\Theta_2)\big] -2\cos^4(\frac{\pi\epsilon}{2})\sin 2(\Theta_1-\Theta_2)\Big\}^2. \tag{13}$$

The detailed derivation process is given in Appendix B. By the Taylor expansion, $P_2(\epsilon)$ can be regrouped as

$$P_2(\epsilon) = \alpha_{2,0} + \alpha_{2,2}\epsilon^2 + O(\epsilon^4), \tag{14}$$

where the expressions of the first two coefficients read

$$\alpha_{2,0} = \sin^2\big[2(\Theta_1-\Theta_2)\big],$$

$$\alpha_{2,2} = \pi^2\sin 2(\Theta_2-\Theta_1)\Big[\sin 2(\Theta_1-\Theta_2) +2\cos\Theta_2\sin\Theta_1+\frac{1}{2}\sin 2\Theta_1+\frac{1}{2}\sin\Theta_2\Big].$$

In the two-pulses sequence, we need to simultaneously solve the following equations:

$$\begin{cases} \alpha_{2,0} = 1, & (15)\\ \alpha_{2,2} = 0. & (16)\end{cases}$$

After some calculations, one solution of Eqs. (15) and (16) can be written as

$$\Theta_1 = m\pi+\frac{\pi}{8},\ \Theta_2 = l\pi+\frac{3\pi}{8}, \tag{17}$$

where m and l are arbitrary integers. By this choice of Θ_1 and Θ_2, the transition probability is accurate to the fourth order in the pulse area error ϵ,

$$P_2(\epsilon) = 1+O(\epsilon^4). \tag{18}$$

The gray solid curve in Fig. 2(a) represents the relation between the transition probability and the pulse area error when $\Theta_1 = \pi/8$ and $\Theta_2 = 3\pi/8$. The result shows that the transition probability appears as a small flat top profile against the pulse area error in the two-pulses sequence. Correspondingly, the gray solid curve in Fig. 2(b) demonstrates that the inversion error in the two-pulses sequence is much lower than that in the single pulse under the same condition. Obviously, the two-pulses sequence has a better fault tolerance than the single pulse in the error-prone environment.

Note that the above designed sequence can also used for implementing a NOT gate with a well-defined phase. Although the phases are inessential for population inversion, they play a very important role when achieving a quantum gate because different phases would determine different types of quantum gates. For our objective, by the group of solution $\Theta_1 = \pi/8$ and $\Theta_2 = 3\pi/8$ and the phase difference $\Psi_n = \pi/2$, the final propagator in the basis $\{|g\rangle, |f\rangle\}$ becomes (up to a global phase)

$$U^{(2)} = \begin{bmatrix} 0 & 1\\ 1 & 0\end{bmatrix},$$

which is actually the X gate. However, when the phase difference is chosen as $\Psi_n = \pi$, the final propagator would become

$$U^{(2)} = \begin{bmatrix} 0 & -i\\ i & 0\end{bmatrix},$$

which is the Y gate; see Appendix B for details.

Furthermore, this current sequence is readily extended to yield an arbitrary rotation gate. The general form of an arbitrary rotation gate in the basis $\{|g\rangle, |f\rangle\}$ is [9]

$$\hat{R} = \begin{bmatrix} \cos(\theta/2)e^{i\beta'} & \sin(\theta/2)e^{i\beta}\\ -\sin(\theta/2)e^{-i\beta} & \cos(\theta/2)e^{-i\beta'}\end{bmatrix},$$

where θ is the rotation angle ($0 \le \theta \le \pi$), and β and β' are relative phases. To implement this rotation gate, Eq. (15) needs to be modified as $\alpha_{2,0} = \sin^2(\theta/2)$, and then we properly adjust the phases of the coupling strengths. As an example, to implement the Hadamard gate by the two-pulses sequence, we first need to obtain a maximum superposition state of $|g\rangle$ and $|f\rangle$, and the equations read

$$\begin{cases} \alpha_{2,0} = 1/2,\\ \alpha_{2,2} = 0.\end{cases}$$

One group of the solutions is $\Theta_1 = 0.1047$ and $\Theta_2 = 0.4974$. Then, we need to choose two proper phases $\phi_n = \varphi_n$, and obtain the Hadamard gate

$$H = \frac{1}{\sqrt{2}}\begin{bmatrix} 1 & 1\\ -1 & 1\end{bmatrix}.$$

Note that different from the previous work [81] for the Hadamard gate in the three-level system, the total pulse area of the current sequence can be 4π, while it is 6π for the sequence $\mathcal{H}_6$ in Ref. [81]. This flexibility of the sequence length benefits from the current sequence starting straight from the three-level system rather than nesting the existing sequence.

B. Three pulses

The three-pulses sequence produce the following propagator:

$$U^{(3)} = U_3(\Theta_3)U_2(\Theta_2)U_1(\Theta_1). \tag{19}$$

Thus, the exact expression of the transition probability $P_3(\epsilon)$ can be written as

$$P_3(\epsilon) = \Big\{\sin2\Theta_3(\sin2\Theta_1\sin2\Theta_2 - 2\sin\Theta_1\sin\Theta_2\sin\pi\epsilon\sin2\pi\epsilon) + 8\cos^2\Theta_1\big[\cos\Theta_2\sin\Theta_3\cos(\Theta_2-\Theta_3) + \sin\Theta_2\cos\Theta_3\sin^2\pi\epsilon\big]$$
$$+4\sin^2\Theta_3\big[\sin2\Theta_1\sin^2\Theta_2 + 2\sin\Theta_1\cos\Theta_2\sin^2\pi\epsilon\big] - 4\sin^2\pi\epsilon(\sin2\Theta_1\cos\Theta_2\cos\Theta_3 - 4\sin\Theta_1\sin\Theta_2\sin2\Theta_3)$$
$$-\cos\pi\epsilon\big[\sin2\Theta_1 + \sin2(\Theta_1-\Theta_2) + \sin2(\Theta_1-\Theta_3) - 3\sin2(\Theta_1-\Theta_2+\Theta_3) + 4\sin\Theta_2\cos\Theta_3\cos(\Theta_2-\Theta_3)$$
$$+8\sin\Theta_1\cos\Theta_3\sin^2\pi\epsilon(\cos(\Theta_1-\Theta_2) + \cos\Theta_2\cos\Theta_3 + 1)\big] - \cos^2\pi\epsilon\big[\sin2\Theta_1 + \sin2\Theta_2 + \sin2\Theta_3 - \sin2(\Theta_1-\Theta_2)$$
$$-\sin2(\Theta_1-\Theta_3) - \sin2(\Theta_2-\Theta_3) - 3\sin2(\Theta_1-\Theta_2+\Theta_3)\big] + 8\cos^3\pi\epsilon\sin\Theta_1\cos\Theta_3\cos(\Theta_1-\Theta_2)\cos(\Theta_2-\Theta_3)\Big\}^2.$$

Similarly, through the Taylor expansion, the transition probability $P_3(\epsilon)$ can be expanded as

$$P_3(\epsilon) = \alpha_{3,0} + \alpha_{3,2}\epsilon^2 + \alpha_{3,4}\epsilon^4 + O(\epsilon^6). \tag{20}$$

Since only three parameters $\{\Theta_1, \Theta_2, \Theta_3\}$ are contained in the three-pulses sequence, it is sufficient to extend Eq. (10) to the fourth-order term. The expressions of the first three coefficients are

$$\alpha_{3,0} = \sin^2 2(\Theta_1 - \Theta_2 + \Theta_3),$$
$$\alpha_{3,2} = -\frac{\pi^2}{2}\sin2(\Theta_1-\Theta_2+\Theta_3)\Big\{\sin2(\Theta_1-\Theta_2) + 2\cos(\Theta_1-\Theta_2)\sin(\Theta_1+\Theta_2-2\Theta_3) + 3\sin2(\Theta_1-\Theta_2+\Theta_3)$$
$$+4\sin\Theta_1\cos(\Theta_2-2\Theta_3) + 4\cos\Theta_3\big[\sin(2\Theta_1-\Theta_2) + \sin\Theta_1\big]\Big\}, \tag{21}$$
$$\alpha_{3,4} = \frac{\pi^4}{48}\Big\{48\big[\sin\Theta_1\cos(\Theta_2-2\Theta_3) + \sin(2\Theta_1-\Theta_2)\cos\Theta_3 + \sin\Theta_1\cos\Theta_3 + \cos(\Theta_1-\Theta_2)\sin(\Theta_1-\Theta_3)\cos(\Theta_2-\Theta_3)$$
$$+51\sin^2 2(\Theta_1-\Theta_2+\Theta_3)\big]^2 + 2\sin2(\Theta_1-\Theta_2+\Theta_3)\big[64\sin\Theta_1\cos(\Theta_2-2\Theta_3) + 4\cos\Theta_3\big[16\sin(2\Theta_1-\Theta_2) + 19\sin\Theta_1$$
$$+3\sin\Theta_2\big] + 64\cos(\Theta_1-\Theta_2)\sin(\Theta_1-\Theta_3)\cos(\Theta_2-\Theta_3) + 12\sin\Theta_1\cos\Theta_2 + 3(\sin2\Theta_1 + \sin2\Theta_2 + \sin2\Theta_3)\big]\Big\}.$$

Therefore, in the three-pulses sequence, the solutions need to simultaneously satisfy the following equations:

$$\begin{cases} \alpha_{3,0} = 1, & (22)\\ \alpha_{3,2} = 0, & (23)\\ \alpha_{3,4} = 0. & (24)\end{cases}$$

Here, the solution for Eq. (22) can be written as $\Theta_1 - \Theta_2 + \Theta_3 = \pi/4 + m\pi/2$, where m is an arbitrary integer. However, it is difficult to derive analytical formulas for Eqs. (23) and (24). Instead, we employ the numerical method to obtain the solutions of Eqs. (22)–(24). One numerical solution is presented in Table I. We figure out the profile of the transition probability $P_3(\epsilon)$ by the blue dashed curves in Figs. 2(a) and 2(b). Clearly, the three-pulses sequence produces a wider top platform than the two-pulses sequence because the fourth-order coefficient α_{34} vanishes. In this situation, the transition probability is accurate to the sixth order in the pulse area error ϵ,

$$P_3(\epsilon) = 1 + O(\epsilon^6). \tag{25}$$

C. More than three pulses

Next, we briefly present the multiple-pulses design procedure. The derivations of the sequence with larger pulse numbers are similar to the two-(three)-pulses sequence. At first, the total propagator of the N-pulses sequence is

$$U^{(N)} = U_N(\Theta_N)U_{N-1}(\Theta_{N-1})\ldots U_1(\Theta_1). \tag{26}$$

In the N-pulses sequence, the transition probability could be expanded to $(2N)$th order by the Taylor expansion

$$P_N(\epsilon) = \alpha_{N,0} + \alpha_{N,2}\epsilon^2 + \alpha_{N,4}\epsilon^4 + \cdots + O(\epsilon^{2N}). \tag{27}$$

It is not hard to find that the zeroth coefficient $\alpha_{N,0}$ can be expressed by (see Appendix A for details)

$$\alpha_{N,0} = \sin^2\left[2\sum_{k=1}^{N}(-1)^{k+1}\Theta_k\right]. \tag{28}$$

Therefore, the solution of the equation $\alpha_{N,0} = 1$ can be written as

$$\sum_{k=1}^{N}(-1)^{k+1}\Theta_k = \frac{\pi}{4} + \frac{m\pi}{2},$$

TABLE I. Values of the coupling strength ratio to achieve population inversion.

N	2	3	4	5	6	7
Θ_1	0.3927	0.1944	0.0897	0.0477	0.0203	0.0137
Θ_2	1.1781	0.7854	0.4688	0.2913	0.1508	0.1072
Θ_3	–	1.3764	1.0613	0.7854	0.5004	0.3811
Θ_4	–	–	1.4676	1.2795	0.9948	0.8233
Θ_5	–	–	–	1.5231	1.3826	1.2459
Θ_6	–	–	–	–	1.5431	1.4854
Θ_7	–	–	–	–	–	1.5606

where m is an arbitrary integer.

Then, the remaining $(N-1)$ equations to be solved come from Eqs. (11). In this situation, the maximum transition probability is accurate to the $(2N)$th order in the pulse area error ϵ,

$$P_N(\epsilon) = 1 + O(\epsilon^{2N}). \tag{29}$$

We present some numerical solutions of Θ_n in Table I, and plot in Figs. 2(a) and 2(b) the performance of the maximum transition probability produced by the four pulses to the seven pulses. As expected, the more pulses we apply, the broader region of the high fidelity against the pulse area error we will get. For example, the inversion error $1 - P_N(\epsilon)$ still remains below 10^{-4} even though the pulse area error reaches 0.328 in the seven-pulses sequence.

D. The influence of waveform deformation

In the ideal situation, the waveform of CPs is the perfect square wave. Unfortunately, the limitations of experimental conditions would produce imperfect pulse shapes in practice. The main problem is the waveform deformation, which usually takes place at the moment of the square wave switching, reflected in the strength jump delay, i.e., the rise and fall edges. As a result, the quantum system is approximately driven by a time-dependent pulse instead of constant pulses sequence. Here, taking the three-pulses sequence for example, we study this issue by designing a function to simulate the imperfect square pulse waveform, and the expression of the coupling strength is

$$\Omega(t) = \begin{cases} \Omega_2 - \dfrac{\Omega_2 - \Omega_1}{1+e^{\tau(t-t_1)}}, & t \le \dfrac{T+t_1-t_3}{2}, \\ \Omega_3 - \dfrac{\Omega_3 - \Omega_2}{1+e^{\tau(t-t_1-t_2)}}, & \dfrac{T+t_1-t_3}{2} < t \le T, \end{cases} \tag{30}$$

where τ is called the waveform deformation parameter and $t_n = 2\pi/\sqrt{\Omega_n^2 + \lambda_n^2}$, $n = 1, 2, 3$.

It is easily found from Eq. (30) that one can control the width of the rising and falling edges by adjusting the dimensionless parameter τ. When the value of τ is larger, the sequence given by Eq. (30) is much closer to the constant pulses sequence. For example, it is shown by the red solid curve in Fig. 3(a) that the deformation degree of the square wave is already negligible when $\tau = 100$. When $\tau \to +\infty$, Eq. (30) describes the perfect square wave. However, when the value of τ is sufficiently small, the waveform described by Eq. (30) is quite different from the perfect square wave, as shown by the blue dotted curve in Fig. 3(a). We plot in Fig. 3(b) the transition probability as a function of the pulse area error and the waveform deformation. The results demonstrate that a slight waveform deformation has little influence on our scheme since the width of the high transition probability region almost remains unchanged when $\tau > 10$. A noticeable change appears in the transition probability only when the waveform deformation is very severe. However, the transition probability still maintains at a high level. Hence, our scheme is also robust against the waveform deformation.

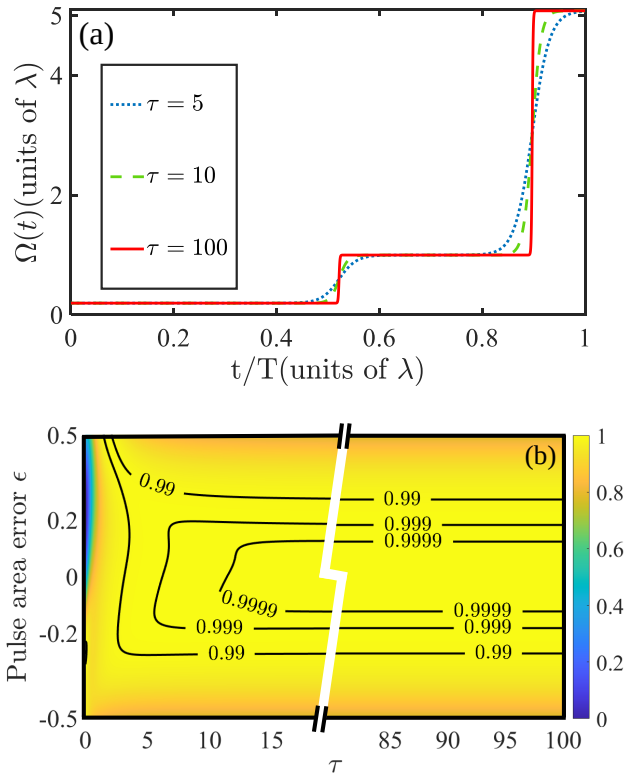

FIG. 3. (a) The waveform of the coupling strength $\Omega(t)$ with different deformation degree in the three-pulses sequence. (b) The maximum transition probability $P_3(\epsilon)$ vs the deformation parameter τ and the pulse area error ϵ. All Θ_n come from Table I.

E. Comparison with other composite pulses

In this section, we make a brief comparison of our CPs sequence with some previous works. First, most previous works [68, 71–73, 81] are based on phase modulation, in which the phase is a time-dependent variable parameter. Different from the phase modulation, here we propose a distinct modulation method: coupling strength modulation, where all phases of the system remain unchanged during the evolution process. Second, the detuning modulation is equivalent to the strength modulation, in principle, since two categories of the Hamiltonian can be associated through a rotation transformation [98].

The common starting point of the current sequence and the sequence in Ref. [81] is to provide robustness against the pulse area error in the three-level system. With the same total pulse area, the robustness of our

composite sequence agrees with that of the composite sequence in Ref. [81]. However, there are some differences between them. At first, the structure of the sequences is distinct. We have only three pulses, while there are six pulses in Ref. [81] with the same pulse area. From the perspective of the waveform, our sequence is a simpler one because it contains fewer pulse jumps. Furthermore, the design procedures are quite different. The sequence in Ref. [81] is constructed by the combination of a preexisting CPs sequence in two-level systems [72], ignoring the dynamics of the excited state. Here, we consider the dynamics of all states in the three-level system, and directly design the composite pulses sequence according to the propagator. Finally, the application systems are different, since we use strength modulation here, while the sequence in Ref. [81] relies on phase modulation. To be specific, one could adopt the phase modulation in some systems with easily adjustable phases (e.g., the trapped ions system [70]) while the strength modulation could be conveniently applied in systems with uncontrollable phases (e.g., the integrated photonic circuits [99]).

For the strength modulation, the difference between the two-level system and the three-level system is mainly embodied in the number of modulation parameters. There are two adjustable coupling strengths in the three-level system, while there is only single coupling strength in the two-level system. When the pulse area is fixed, one cannot eliminate the error by only modulating the coupling strength in a two-level system [71]. In order to make this strength modulation valid, one must also modulate the pulse area, as done in Ref. [80]. However, this situation is quite different in the three-level system. Without a change in the pulse area, we can modulate the ratio of two coupling strengths to effectively eliminate the systematic errors.

Moreover, the SMCPs in Ref. [80] focuses on altering the exchange coupling to achieve robust quantum control in the singlet-triplet qubit. This kind of pulse sequence needs to nest amounts of short pulses. Hence, the pulse length would be long and may not maintain a high-fidelity performance in the decoherence environment. In our scheme, the pulse length can be appropriately chosen to equilibrate between pulse duration and robustness. On the other hand, the SMCPs in Ref. [85] are designed for suppressing leakage in the three-level system. This scheme [85] is required to simultaneously include two modulation parameters, including the on-site potentials and the tunneling coupling. In the current scheme, only one of the coupling strengths is sufficient to be modulated to implement robust quantum control, while another coupling strength remains unchanged during the evolution process.

IV. ILLUSTRATIVE EXAMPLE

In this section, we mainly illustrate the applications of the current SMCPs sequence for concrete physical models. This current sequence is suitable for some systems where the phase is hardly to be modulated. For example, in integrated photonic circuits [99], since the coupling parameters between different waveguides are real valued, the traditional phase modulation CPs is unapplicable. During the light transportation process from one waveguide to another, one can alter the spatial distance between waveguides, which is recognized as one kind of strength modulation between different waveguides. And the amount of light coupling from one waveguide to the other can be tuned by lithographically adjusting their width [99]. Thus, one can adopt strength modulation CPs to achieve robust light transportation between different waveguides in integrated photonic circuits [78].

The current sequence is also feasible for the system where the strength parameters are conveniently modulated. For instance, in the system consisting of multiple quantum dots [100], there are two strength parameters involved in the control of quantum dots at the same time. One is the chemical potential of quantum dots, which is used for modulating the detuning. The other is the tunneling barrier between adjacent quantum dots, which alters the coupling of quantum dots. Note that both strength parameters can be appropriately controlled by adjusting gate voltages, taking advantage of short-range interaction and electrical controllability [100]. Therefore, a proper value of the gate voltage would make two quantum dots couple efficiently and produce a time-dependent exchange. So it is convenient for employing the strength modulation in this system.

In the superconducting circuits system [101], both the strength modulation and the phase modulation can be used to achieve robust quantum control by modulating the interaction of external fields. When considering the weak dephasing in this system, the phase modulation method [76] is less robust against the phase noise than the strength modulation method. Thus, systematic errors may not be effectively eliminated due to the dephasing, and this problem can be elegantly circumvented by the current SMCPs sequence. In the following, we choose this system to illustrate how to achieve robust quantum control by our SMCPs sequence.

The superconducting quantum interference devices (SQUIDs) are elementary components in superconducting circuits [102–107], and the energy level of the SQUID qubits can be easily modulated by changing the local bias fields [101]. As shown in Fig. 4(a), the Hamiltonian of each SQUID qubit has the following form [103, 104]:

$$H_{SQUID}=\frac{Q^2}{2C}+\frac{(\mathbf{\Phi}-\mathbf{\Phi}_x)^2}{2L}-E_J\cos(2\pi\frac{\mathbf{\Phi}}{\mathbf{\Phi}_0}), \quad (31)$$

where C is the junction capacitance, L is the loop inductance, Q is the total charge on the capacitor, $\mathbf{\Phi}$

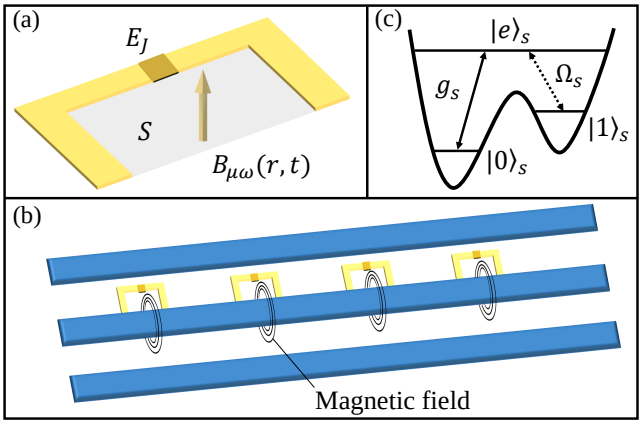

FIG. 4. (a) Schematic diagram of the SQUID qubit. (b) Four SQUID qubits coupled to a single-mode cavity field. (c) The energy-level configuration of every SQUID qubit.

is the magnetic flux through the loop, $\mathbf{\Phi}_x$ is the external flux applied to the loop, $\mathbf{\Phi}_0 = h/2e$ is the flux quantum, and $E_J = I_c\mathbf{\Phi}_0/2\pi$ is the Josephson energy with I_c being the critical current of the junction.

Consider the system of four SQUID qubits coupled to a single-mode microwave cavity field, as shown in Fig. 4(b). Every SQUID qubit has a three-level structure with three states $\{|0\rangle_s, |1\rangle_s, |e\rangle_s\}(s = 1, 2, 3, 4)$, as shown in Fig. 4(c), where $|0\rangle_s$ and $|1\rangle_s$ are two ground states and $|e\rangle_s$ is the excited state. The ground state $|0\rangle_s$ resonantly couples to the excited state $|e\rangle_s$ by the cavity field with the constant strength g_s. The classical field resonantly drives the transition between the states $|1\rangle_s$ and $|e\rangle_s$ with the coupling strength Ω_s. The general forms of coupling strength Ω_s and the coupling constant g_s are given by [103, 104]

$$\Omega_s = \frac{1}{2L_s\hbar}\langle 1|\mathbf{\Phi}|e\rangle_s \int_{S_s} \mathbf{B}^s_{\mu w}(\mathbf{r},t)\cdot d\mathbf{S}, \tag{32}$$

$$g_s = \frac{1}{L_s}\sqrt{\frac{\omega_c}{2\mu_0\hbar}}\langle 0|\mathbf{\Phi}|e\rangle_s \int_{S_s} \mathbf{B}^s_c(\mathbf{r})\cdot d\mathbf{S}, \tag{33}$$

where S_s is the surface surrounded by the ring of the sth SQUID, L_s is the loop inductance of the sth SQUID, ω_c is the angular frequency of the cavity, and μ_0 is magnetic permeability in a vacuum. $\mathbf{B}^s_c(\mathbf{r})$ is the magnetic component of the normal cavity mode. $\mathbf{B}^s_{\mu w}(\mathbf{r},t)$ is the magnetic component of the classical field.

From Eqs. (32) and (33), one finds that the coupling strength Ω_s and the coupling constant g_s can be controlled by the microwave magnetic components $\mathbf{B}^s_{\mu w}(\mathbf{r},t)$ and the magnetic component $\mathbf{B}^s_c(\mathbf{r})$ of the normal cavity mode, respectively. Due to the spatial inhomogeneity of the magnetic fields, there may exist uncertainty in Ω_s and g_s. On the other hand, the distorted pulse shape or inexact evolution time could also produce uncertainty in the pulse area. Consequently, the quantum operations would lose accuracy in this system. To eliminate those uncertainties, we can employ the SMCPs scheme to prepare the W state with high fidelity, which is actually to control the microwave magnetic components $\mathbf{B}^s_{\mu w}(\mathbf{r},t)$, in practice. In the following, we adopt η_1 and η_2 to represent the uncertainties from $\mathbf{B}^s_{\mu w}(\mathbf{r},t)$ and $\mathbf{B}^s_c(\mathbf{r})$, respectively. The Hamiltonian of the whole system in the interaction picture is ($\hbar = 1$) [105]

$$H_I = H_m + H_c, \tag{34}$$

$$H_m = \frac{1}{2}\sum_{s=1}^{4}\left[\Omega_s(1+\eta_1)|e\rangle_s\langle 1| + \text{H.c.}\right], \tag{35}$$

$$H_c = \frac{1}{2}\sum_{s=1}^{4}\left[g_s(1+\eta_2)|e\rangle_s\langle 0|\hat{a} + \text{H.c.}\right], \tag{36}$$

where $\hat{a}$ is the annihilation operator of the cavity field. H_c (H_m) describes the interaction between the cavity (classical) fields and the SQUID qubits.

Note that the excited number is a conserved quantity in this system because the excited number operator $\hat{N}_e = \sum_s(|e\rangle_s\langle e| + |1\rangle_s\langle 1|) + \hat{a}^\dagger\hat{a}$ satisfies $[\hat{N}_e, H_I] = 0$. Therefore, we can restrict the system dynamics in the single excited subspace, namely, $\langle\psi(t)|\hat{N}_e|\psi(t)\rangle = 1$, where $|\psi(t)\rangle$ is the evolution state of the system. The bases of the single excited subspace are

$$\begin{aligned}
|\psi_1\rangle &= |0\rangle_1|0\rangle_2|0\rangle_3|1\rangle_4|0\rangle_c, & |\psi_2\rangle &= |0\rangle_1|0\rangle_2|0\rangle_3|e\rangle_4|0\rangle_c,\\
|\psi_3\rangle &= |0\rangle_1|0\rangle_2|0\rangle_3|0\rangle_4|1\rangle_c, & |\psi_4\rangle &= |e\rangle_1|0\rangle_2|0\rangle_3|0\rangle_4|0\rangle_c,\\
|\psi_5\rangle &= |0\rangle_1|e\rangle_2|0\rangle_3|0\rangle_4|0\rangle_c, & |\psi_6\rangle &= |0\rangle_1|0\rangle_2|e\rangle_3|0\rangle_4|0\rangle_c,\\
|\psi_7\rangle &= |1\rangle_1|0\rangle_2|0\rangle_3|0\rangle_4|0\rangle_c, & |\psi_8\rangle &= |0\rangle_1|1\rangle_2|0\rangle_3|0\rangle_4|0\rangle_c,\\
|\psi_9\rangle &= |0\rangle_1|0\rangle_2|1\rangle_3|0\rangle_4|0\rangle_c.
\end{aligned}$$

For simplicity, we set $g_1 = g_2 = g_3 = g$, $g_4 = \sqrt{3}g$. This could be realized by properly adjusting the parameters of the SQUIDs, such as L_s or S_s. Then, we rewrite the Hamiltonian H_c given by Eq. (36) in this set of basis, i.e.,

$$\begin{aligned}
H_c =& g(1+\eta_2)(|\psi_4\rangle + |\psi_5\rangle + |\psi_6\rangle)\langle\psi_3|\\
&+ \sqrt{3}g(1+\eta_2)|\psi_2\rangle\langle\psi_3| + \text{H.c.},
\end{aligned} \tag{37}$$

and the eigenstates of the Hamiltonian H_c are

$$|\phi_1\rangle = -\frac{1}{\sqrt{2}}\left[|\psi_2\rangle - \frac{1}{\sqrt{3}}(|\psi_4\rangle + |\psi_5\rangle + |\psi_6\rangle)\right], \tag{38}$$

$$|\phi_2\rangle = \frac{1}{2}\left[|\psi_2\rangle + \sqrt{2}|\psi_3\rangle + \frac{1}{\sqrt{3}}(|\psi_4\rangle + |\psi_5\rangle + |\psi_6\rangle)\right], \tag{39}$$

$$|\phi_3\rangle = \frac{1}{2}\left[|\psi_2\rangle - \sqrt{2}|\psi_3\rangle + \frac{1}{\sqrt{3}}(|\psi_4\rangle + |\psi_5\rangle + |\psi_6\rangle)\right], \tag{40}$$

with the corresponding eigenvalues $E_1 = 0$, $E_2 = \sqrt{6}g$, and $E_3 = -\sqrt{6}g$. Remarkably, $|\phi_1\rangle$ is the dark state of this system. Next, we set $\Omega_1 = \Omega_2 = \Omega_3 = \sqrt{2}\Omega_a$ and $\Omega_4 = \sqrt{2}\Omega_b$, and the Hamiltonian H_I of the whole system

given by Eq. (34) can be rearranged into a new form,

$$H_I' = H_c' + H_m', \tag{41}$$

$$H_c' = \sum_{i=1}^{3} E_i|\phi_i\rangle\langle\phi_i|, \tag{42}$$

$$\begin{aligned} H_m' = &\frac{\Omega_a}{\sqrt{2}}(1+\eta_1)\big(|\phi_2\rangle+|\phi_3\rangle\big)\langle\psi_1|+\Omega_a(1+\eta_1)|\phi_1\rangle\langle\psi_1| \\ &+\frac{\Omega_b}{\sqrt{2}}(1+\eta_1)\big(|\phi_2\rangle+|\phi_3\rangle\big)\langle\psi_f|+\Omega_b(1+\eta_1)|\phi_1\rangle\langle\psi_f| \\ &+\text{H.c.}, \end{aligned} \tag{43}$$

where $|\psi_f\rangle = (|\psi_7\rangle + |\psi_8\rangle + |\psi_9\rangle)/\sqrt{3}$. Finally, we perform the unitary transformation $U = e^{-iH_c't}$ on this system, and the Hamiltonian H_I' given by Eq. (41) can be rewritten as

$$\begin{aligned} H_I'' = &\frac{\Omega_a}{\sqrt{2}}(1+\eta_1)\Big(e^{i\sqrt{6}gt}|\phi_2\rangle + e^{-i\sqrt{6}gt}|\phi_3\rangle\Big)\langle\psi_1| \\ &+\frac{\Omega_b}{\sqrt{2}}(1+\eta_1)\Big(e^{i\sqrt{6}gt}|\phi_2\rangle + e^{-i\sqrt{6}gt}|\phi_3\rangle\Big)\langle\psi_f| \\ &+\Omega_a(1+\eta_1)|\phi_1\rangle\langle\psi_1|+\Omega_b(1+\eta_1)|\phi_1\rangle\langle\psi_f| + \text{H.c.} \end{aligned} \tag{44}$$

Figure 5 shows the transition paths for the system governed by the Hamiltonian H_I''. When the system parameters satisfy the condition $\Omega_{a,b} \ll g$, the high-frequency oscillation terms $e^{\pm i\sqrt{6}gt}$ can be safely ignored. Then, both the transition paths $|\psi_1\rangle \leftrightarrow |\phi_2\rangle \leftrightarrow |\psi_f\rangle$ and $|\psi_1\rangle \leftrightarrow |\phi_3\rangle \leftrightarrow |\psi_f\rangle$ are effectively suppressed, and only the transition path $|\psi_1\rangle \leftrightarrow |\phi_1\rangle \leftrightarrow |\psi_f\rangle$ is feasible. As a result, the whole system is simplified into a Λ-type physical model, and the effective Hamiltonian, in the basis $\{|\psi_1\rangle, |\psi_f\rangle, |\phi_1\rangle\}$, reads [105]

$$H_e = (1+\eta_1)\begin{bmatrix} 0 & 0 & -\Omega_a \\ 0 & 0 & \Omega_b \\ -\Omega_a & \Omega_b & 0 \end{bmatrix}, \tag{45}$$

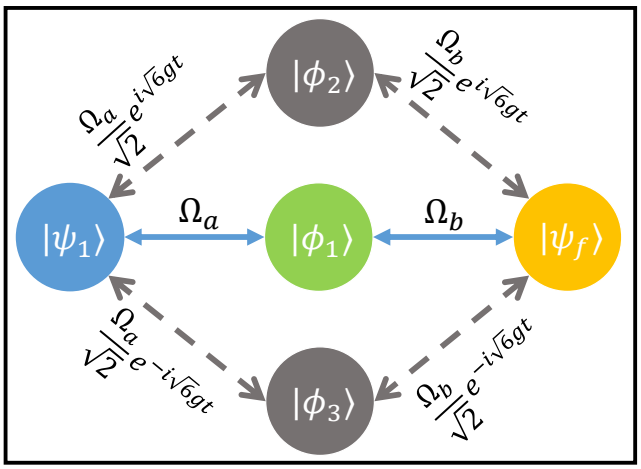

FIG. 5. Schematic diagram of transition paths for the Hamiltonian H_I'' given by Eq. (44).

where

$$|\psi_f\rangle = \frac{1}{\sqrt{3}}(|1\rangle_1|0\rangle_2|0\rangle_3+|0\rangle_1|1\rangle_2|0\rangle_3+|0\rangle_1|0\rangle_2|1\rangle_3)\otimes|0\rangle_4|0\rangle_c$$

is the W state. Therefore, the SMCPs scheme studied in Sec. III can be directly employed to the effective Hamiltonian given by Eq. (45) to prepare the W state $|\psi_f\rangle$. Moreover, we can expect that the influence caused by the uncertainty of the cavity field can be negligible during the evolution process because η_2 does not appear in the effective Hamiltonian given by Eq. (45).

In Figs. 6(a)–6(d), we plot the fidelity of the W state as a function of the uncertainties η_1 and η_2 with different pulses sequence, where we set $\Omega_{max} = \max\{\Omega_{na}, \Omega_{nb}\}$ and $g/\Omega_{max} = 7$. The numerical results verify that the uncertainty of the coupling constant g has a negligible effect on the final fidelity, since the fidelity almost remains unchanged with the increase of η_2. Note that the fidelity obviously changes when $\eta_2 < -0.5$. This is because the condition $g \gg \Omega_{a,b}$ is no longer satisfied very well. As a result, the effective Hamiltonian given by Eq. (45) is invalid in this regime. On the other hand, the fidelity is also robust against the uncertainty of the coupling strength of the classical fields since the fidelity still keeps a relatively high value even though $\eta_1 = \pm 0.2$. Thus, we can achieve the W state in a robust way even when there are existing uncertainties in the superconducting circuits.

Next, we turn to study the influence of waveform deformation on the fidelity of the W state. We take the three-pulses sequence as an example, and plot in Fig. 7 the infidelity as a function of the pulse area error and the waveform deformation. An inspection

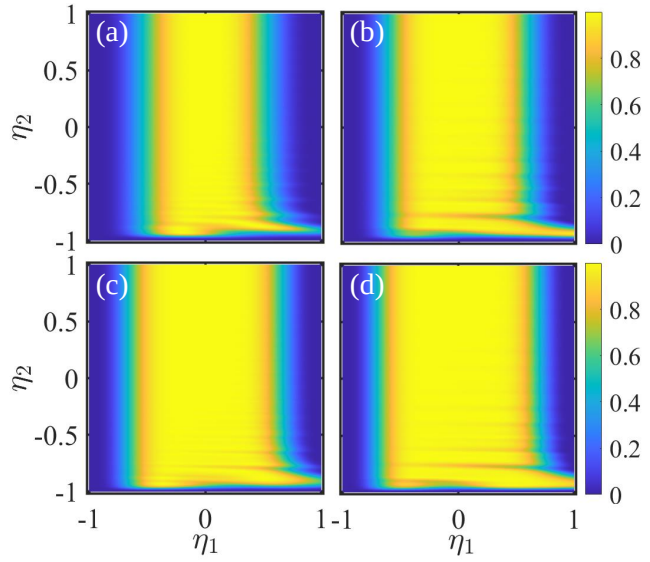

FIG. 6. The fidelity F of the W state vs two kinds of the uncertainties η_1 and η_2 in the (a) two-pulses, (b) three-pulses, (c) four-pulses, and (d) five-pulses sequence. $g/\Omega_{max} = 7$. $\tau = 10^3$. All Θ_n come from Table I.

of Fig. 7 demonstrates that the scheme is insensitive to waveform deformation, even in the case of severe deformation, because the W state still maintains a high fidelity in the region $\tau > 3$. Hence, our scheme can resist the imperfection of input waveform and thus give more flexibility in terms of input waveform conditions.

Until now, we have not investigated the influence of decoherence on the fidelity of the W state. When considering the decoherence induced by the cavity decay, the spontaneous emission, and the dephasing, the evolution of this system can be governed by the Lindblad master equation,

$$\dot{\rho} = i[\rho, H_I] + \mathcal{L}(\sqrt{\kappa}\hat{a})\rho + \sum_{l=0}^{1}\sum_{s=1}^{4}\Big[\mathcal{L}(\hat{\sigma}_{le}^{s})\rho + \mathcal{L}(\hat{\sigma}_{ee,ll}^{s})\rho\Big], \tag{46}$$

where $\hat{\sigma}_{le}^{s} = \sqrt{\gamma_{ls}}|l\rangle_s\langle e|$, $\hat{\sigma}_{ee,ll}^{s} = \sqrt{\gamma_{ls}^{\phi}/2}(|e\rangle_s\langle e| - |l\rangle_s\langle l|)$, and the general form of the superoperator is

$$\mathcal{L}(\hat{o})\rho = \hat{o}\rho\hat{o}^{\dagger} - \frac{1}{2}(\hat{o}^{\dagger}\hat{o}\rho + \rho\hat{o}^{\dagger}\hat{o}). \tag{47}$$

Here, $\hat{o}$ denotes the standard Lindblad operator, κ is the decay rate of the cavity field, and γ_{ls} (γ_{ls}^{ϕ}) represent the dissipation (dephasing) rate from the excited state $|e\rangle$ to the ground state $|l\rangle$.

Figures 8(a)–8(c) demonstrate the relationship between the fidelity of the W state and the decoherence parameters $\{\gamma, \gamma^{\phi}, \kappa\}$, where we set $\gamma_{ls} = \gamma$ and $\gamma_{ls}^{\phi} = \gamma^{\phi}$ for simplicity. According to Fig. 8(a) and Fig. 8(c), the fidelity of the W state is hardly affected by the cavity decay. Physically, it is due to the fact that the single-photon state of the cavity field is almost decoupling during the system evolution. We can observe from Fig. 8(a) and Fig. 8(b) that the spontaneous emission of the SQUID qubits has a slight influence on the fidelity of the W state. The reason is as follows. Although $|\phi_k\rangle$ ($k = 1, 2, 3$) contain the excited states of the SQUID qubits, as given by Eqs. (38)–(40), they are almost negligible in the evolution process when satisfying the condition $\Omega_{a,b} \ll g$. This can be verified by Fig. 8(d), which demonstrates that the population of the state $|\phi_k\rangle$ ($k = 1, 2, 3$) is suppressed within an extremely small range during the system evolution. As a result, the current scheme can maintain a high fidelity even when the dissipation rate of the excited state is large.

It is inevitable that the increase of the CPs sequence would prolong the total interaction time and impact the final fidelity under the decoherence environment. In the following, we study this issue. Figure 9(a) shows the results obtained by various pulse lengths under different decoherence environments. In the ideal situation, i.e., $\gamma/g = 0$, the final fidelity almost remains unchanged as the pulse number increases. When considering the decoherence caused by the atomic spontaneous emission and dephasing, e.g., $\gamma/g = 2 \times 10^{-5}$, the final fidelity decreases slightly over an increasing number of pulses. The reason is that a long pulse sequence takes a long interaction time so that the decoherence becomes the main factor in reducing the final fidelity. Hence, to obtain a relatively high fidelity in the decoherence environment, we cannot choose an overlong pulse sequence.

To quantify the robustness under the decoherence environment, we define a benchmark width

$$W_b = \eta_{1,max} - \eta_{1,min}, \tag{48}$$

where $\eta_{1,max(min)}$ is the positive (negative) maximum uncertainty in the coupling strength Ω_s to make the

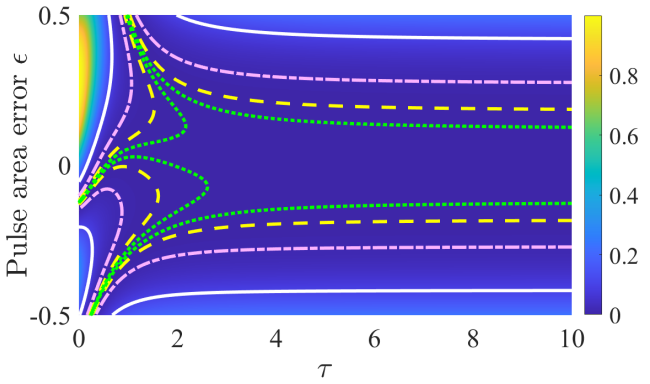

FIG. 7. The infidelity $1-F$ of the W state vs the uncertainty η_1 and the deformation parameter τ in the three-pulses scheme, where $g/\Omega_{max} = 15$. The green dotted curve, the yellow dashed curve, the pink dot-dashed curve, and the white solid curve correspond to the infidelity $1 - F = 10^{-4}$, 10^{-3}, 10^{-2}, and 10^{-1}. All Θ_n come from Table I.

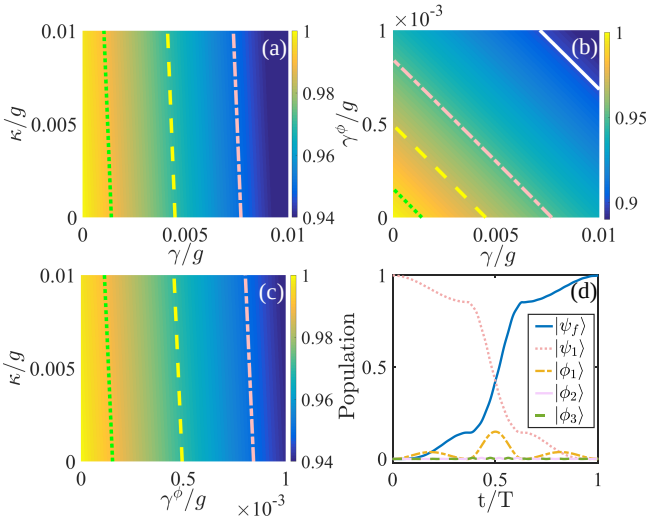

FIG. 8. The fidelity of the W state vs (a) γ/g and κ/g, (b) γ/g and γ^{ϕ}/g, and (c) γ^{ϕ}/g and κ/g in the three-pulses scheme. Here, the green dotted line, the yellow dashed line, the pink dot-dashed line, and the white solid line correspond to the final fidelity $F = 0.99$, 0.97, 0.95, and 0.90. (d) The population evolution of the states $|\phi_k\rangle$, $|\psi_1\rangle$, and $|\psi_f\rangle$ in the three pulses scheme, where the initial state is $|\psi_1\rangle$. $g/\Omega_{max} = 7$ and $\tau = 10^3$. All Θ_n come from Table I.

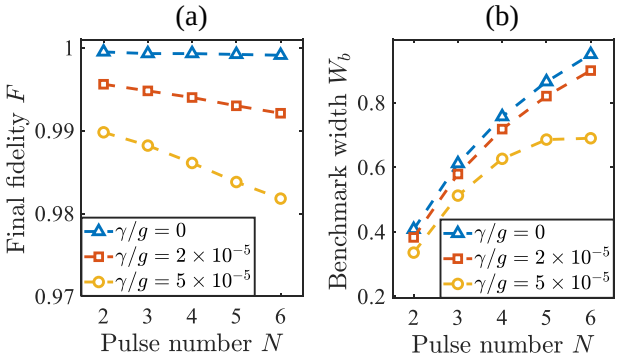

FIG. 9. (a) The final fidelity of the W state and (b) the benchmark width W_b vs different pulse number N. Here we set the benchmark value $F_b = 0.98$ and $\gamma_p = \gamma$. All Θ_n come from Table I. Other parameters are $\kappa/g = 0.01$, $g/\Omega_{max} = 20$, and $\tau = 10^3$.

final fidelity reach a benchmark value F_b. Remarkably, this benchmark width can characterize the robustness against uncertainty provided by different pulse sequences. Figure 9(b) reveals the benchmark widths achieved by different pulse sequences under different decoherence environments. On the one hand, we can find that the too short pulse sequence cannot obtain a remarkable benchmark width (e.g., $W_b = 0.3828$ for $N = 2$ and $\gamma/g = 2 \times 10^{-5}$). On the other hand, the benchmark width becomes wider along with the pulse number increasing, and the increment of W_b becomes gradually limited when the pulse number is large. In other words, when the system suffers from a serious decoherence, we cannot obtain considerable robustness for an overlong sequence (e.g., $W_b = 0.6899$ for $N = 6$ and $\gamma/g = 5 \times 10^{-5}$). From this point of view, to obtain excellent robustness, both a too short pulse sequence and an overlong pulse sequence should not be considered preferentially.

Therefore, we need to choose a moderate pulse length to seek an optimal tradeoff between the final fidelity and robustness (fault tolerance). In recent experiments [101, 108–112], the following parameters are feasible: $\gamma = \gamma^{\phi} \sim 10$kHz and $\kappa \sim 625$kHz. The coupling constant g could reach 600MHz [113], and thus $\gamma/g \sim 1.6667 \times 10^{-5}$. According to these parameters, the final fidelity of the W state can reach 0.9955 by the four-pulses sequence, while the benchmark width is $W_b = 0.7307$ for $F_b = 0.98$. As a result, our scheme still retains good performance in a decoherence environment.

V. CONCLUSION

In summary, we have put forward the SMCPs scheme to achieve robust population inversion in a three-level system. The transition probability is directly derived from a total propagator, and we mainly focus on reducing the influence caused by the pulse area error on the transition probability. By means of the Taylor expansion, we nullify the first few error terms in the transition probability through designing the values of the coupling strengths. We have given the analytical expressions of the coupling strengths in the two-pulses sequence. For the three- and more-than-three-pulses (up to seven-pulses) sequence, we present a set of optimal parameters by numerical methods. These results indicate that the robust manner against the pulse area error can be much better as the pulse number increases. Our scheme provides a feasibility extension of a longer sequence. Meanwhile, this scheme provides a flexible choice to design pulse length in a desirable manner for achieving high robustness against errors and an appropriate total operating time. Moreover, the pulse sequence interfered by waveform deformation is still valid to achieve high transition probability. This property is very useful for the resistance of pulse jump delay. As a result, our SMCPs scheme is robust against the pulse area error and waveform deformations.

Then, we have extended this SMCPs scheme to prepare the W state with high fidelity in the superconducting circuits, where four SQUID qubits are coupled with the cavity field and classical fields. The SMCPs that we design can effectively compensate for the adverse impact caused by waveform deformations and uncertainties in coupling strengths. Furthermore, we also discuss the feasibility and the robustness of this scheme in a decoherence environment. The simulation results show that our scheme can obtain a good performance against the impact of the cavity decay and the spontaneous emission, and we need to select a moderate pulse length to achieve robust and accurate quantum control. We hope that this scheme will provide robust control for more physical models in the future.

ACKNOWLEDGMENTS

This work is supported by the National Natural Science Foundation of China under Grants No. 11874114 and No. 11805036, the Natural Science Foundation of Fujian Province under Grant No. 2021J01575, the Natural Science Funds for Distinguished Young Scholar of Fujian Province under Grant No. 2020J06011, and the Project from Fuzhou University under Grant No. JG202001-2.

Appendix A: Derivation of the propagator for the N pulses sequence in the two-photon resonance regime

In this appendix, we deduce the expression of the propagator without errors when the three-level system works in the two-photon resonance regime, where all parameters are time-independent. The general form of a three-level system Hamiltonian for the nth pulse is given by

$$H_n = \Delta_n|e\rangle\langle e| + \frac{1}{2}\Big(\Omega_n e^{i\phi_n}|g\rangle\langle e| + \lambda_n e^{i\varphi_n}|f\rangle\langle e| + \text{H.c.}\Big), \tag{A1}$$

where Ω_n and ϕ_n (λ_n and φ_n) are the coupling strength and the phase of the transition $|g\rangle \leftrightarrow |e\rangle$ ($|f\rangle \leftrightarrow |e\rangle$), and Δ_n is the single-photon detuning. In this case, the propagator becomes $U_n(\Theta_n) = \exp\left(-iH_nT_n\right)$, where T_n is the pulse duration and $\Theta_n = \arctan(\Omega_n/\lambda_n)$. By selecting the pulse duration $T_n = 2\pi/\sqrt{\Omega_n^2+\lambda_n^2+\Delta_n^2}$, two ground states are decoupled from the excited state $|e\rangle$ so that we only focus on the subspace $\{|g\rangle, |f\rangle\}$. Thus, the matrix form of the propagator $U_n(\Theta_n)$ in the basis $\{|g\rangle, |f\rangle\}$ reads

$$U_n(\Theta_n) = \cos x_n \begin{bmatrix} \cos 2\Theta_n + i\tan x_n & -e^{i\Psi_n}\sin 2\Theta_n \\ -e^{-i\Psi_n}\sin 2\Theta_n & -\cos 2\Theta_n + i\tan x_n \end{bmatrix}, \tag{A2}$$

where the global phase is neglected, and

$$x_n = \frac{\pi\Delta_n}{2\sqrt{1+\Delta_n^2}}, \qquad \Psi_n = \phi_n - \varphi_n.$$

Note that the total propagator for the composite pulses sequence could be obtained by nesting the propagator $U_n(\Theta_n)$ in order. We first start from the two-pulses sequence, and the propagator comes into

$$\begin{aligned} U^{(2)} &= U_2(\Theta_2)U_1(\Theta_1) \\ &= \cos x_1\cos x_2 \begin{bmatrix} \cos 2\Theta_2 + i\tan x_2 & -e^{i\Psi}\sin 2\Theta_2 \\ -e^{-i\Psi}\sin 2\Theta_2 & -\cos 2\Theta_2 + i\tan x_2 \end{bmatrix} \begin{bmatrix} \cos 2\Theta_1 + i\tan x_1 & -e^{i\Psi}\sin 2\Theta_1 \\ -e^{-i\Psi}\sin 2\Theta_1 & -\cos 2\Theta_1 + i\tan x_1 \end{bmatrix} \\ &= \cos x_1\cos x_2 \begin{bmatrix} \cos 2(\Theta_1-\Theta_2) + g_2 & \big[-\sin 2(\Theta_1-\Theta_2) + h_2\big]e^{i\Psi} \\ \big[\sin 2(\Theta_1-\Theta_2) - h_2^*\big]e^{-i\Psi} & -\cos 2(\Theta_1-\Theta_2) + g_2^* \end{bmatrix}, \end{aligned}$$

with

$$\begin{aligned} g_2 &= -\tan x_1\tan x_2 + i\left(\tan x_1\cos 2\Theta_2 + \tan x_2\cos 2\Theta_1\right), \\ h_2 &= -i\left(\tan x_1\sin 2\Theta_2 + \tan x_2\sin 2\Theta_1\right), \end{aligned}$$

where g_2 and h_2 are defined as functions associated with the parameters $\{x_1, x_2, \Theta_1, \Theta_2\}$. Similarly, the propagator of the three-pulses sequence is

$$\begin{aligned} U^{(3)} &= U_3(\Theta_2)U_2(\Theta_2)U_1(\Theta_1) \\ &= \left(\prod_{n=1}^{3}\cos x_n\right) \begin{bmatrix} \cos 2(\Theta_1-\Theta_2+\Theta_3) + g_3 & \big[-\sin 2(\Theta_1-\Theta_2+\Theta_3) + h_3\big]e^{i\Psi} \\ \big[-\sin 2(\Theta_1-\Theta_2+\Theta_3) + h_3^*\big]e^{-i\Psi} & -\cos 2(\Theta_1-\Theta_2+\Theta_3) - g_3^* \end{bmatrix}, \end{aligned}$$

where

$$\begin{aligned} g_3 &= -(\tan x_1\tan x_2\cos 2\Theta_3 + \tan x_1\tan x_3\cos 2\Theta_2 + \tan x_2\tan x_3\cos 2\Theta_1) \\ &\quad + i\big[\tan x_1\cos 2(\Theta_2-\Theta_3) + \tan x_2\cos 2(\Theta_1-\Theta_3) + \tan x_3\cos 2(\Theta_1-\Theta_2) - \tan x_1\tan x_2\tan x_3\big], \\ h_3 &= (\tan x_1\tan x_2\sin 2\Theta_3 + \tan x_1\tan x_3\sin 2\Theta_2 + \tan x_2\tan x_3\sin 2\Theta_1) \\ &\quad - i\big[\tan x_1\sin 2(\Theta_2-\Theta_3) + \tan x_2\sin 2(\Theta_1-\Theta_3) + \tan x_3\sin 2(\Theta_1-\Theta_2)\big]. \end{aligned}$$

Following the above rules, the propagator of the N-pulses sequence could be obtained and reads

$$\begin{aligned} U^{(N)} &= U_N(\Theta_N)U_{N-1}(\Theta_{N-1})\cdots U_1(\Theta_1) \\ &= \left(\prod_{n=1}^{N}\cos x_n\right) \begin{bmatrix} \cos 2\Theta_N + i\tan x_N & -e^{i\Psi}\sin 2\Theta_N \\ -e^{-i\Psi}\sin 2\Theta_N & -\cos 2\Theta_N + i\tan x_N \end{bmatrix} \cdots \begin{bmatrix} \cos 2\Theta_1 + i\tan x_1 & -e^{i\Psi}\sin 2\Theta_1 \\ -e^{-i\Psi}\sin 2\Theta_1 & -\cos 2\Theta_1 + i\tan x_1 \end{bmatrix} \\ &= \left(\prod_{n=1}^{N}\cos x_n\right) \begin{bmatrix} \cos\left(2\sum_{n=1}^{N}(-1)^{n+1}\Theta_n\right) + g_N & \left[-\sin\left(2\sum_{n=1}^{N}(-1)^{n+1}\Theta_n\right) + h_N\right]e^{i\Psi} \\ (-1)^N\left[\sin\left(2\sum_{n=1}^{N}(-1)^{n+1}\Theta_n\right) - h_N^*\right]e^{-i\Psi} & (-1)^N\left[\cos\left(2\sum_{n=1}^{N}(-1)^{n+1}\Theta_n\right) + g_N^*\right] \end{bmatrix}, \end{aligned} \tag{A3}$$

where

$$g_N = \sum_{a=1}^{N-1}\left[\prod_{1\le j_1\le\cdots\le j_a\le N}^{N}(i\tan x_{j_l})\right]\cos\left[\sum_{\substack{1\le j'_1\le\cdots\le j'_{N-a}\le N\\ j_l\neq j'_m}}^{N}(-1)^{(m+1)}\left(2\Theta_{j'_m}\right)\right]+\prod_{n=1}^{N}(i\tan x_n),$$

$$h_N = -\sum_{a=1}^{N-1}\left[\prod_{1\le j_1\le\cdots\le j_a\le N}^{N}(i\tan x_{j_l})\right]\sin\left[\sum_{\substack{1\le j'_1\le\cdots\le j'_{N-a}\le N\\ j_l\neq j'_m}}^{N}(-1)^{(m+1)}\left(2\Theta_{j'_m}\right)\right].$$

We observe from Eq. (A3) that the transition probability of the target state $|f\rangle$ is concurrently controlled by the coupling strengths and detuning. When the system is always in the resonance regime ($\Delta_n = 0$), it is easily found that $\cos x_n = 1$, $g_N = 0$, and $h_N = 0$. Then, the final propagator in the absence of errors becomes very concise, which reads

$$U^{(N)} = \begin{bmatrix} \cos\left[2\sum_{n=1}^{N}(-1)^{n+1}\Theta_n\right] & -\sin\left[2\sum_{n=1}^{N}(-1)^{n+1}\Theta_n\right]e^{i\Psi} \\ (-1)^N\sin\left[2\sum_{n=1}^{N}(-1)^{n+1}\Theta_n\right]e^{-i\Psi} & (-1)^N\cos\left[2\sum_{n=1}^{N}(-1)^{n+1}\Theta_n\right] \end{bmatrix}.$$

As a result, the expression of the transition probability of the target state $|f\rangle$ is

$$P_N = |U_{21}|^2 = \sin^2\left[2\sum_{n=1}^{N}(-1)^{n+1}\Theta_n\right],$$

which is Eq. (32) in the main text. In order to achieve complete population inversion, the ratio of coupling strength for each pulse, obtained by solving the equation $P_N = 1$, must be satisfied, and the solution is

$$\sum_{n=1}^{N}(-1)^{n+1}\Theta_n = \frac{\pi}{4}+\frac{m\pi}{2}, \tag{A4}$$

where m is an arbitrary integer. This is the first condition that Θ_n should be satisfied.

Appendix B: Detailed derivation process in the two pulses sequence

In this appendix, we present the detailed derivation process of the coupling strengths in the two-pulses sequence. When $\Delta = 0$, according to Eq. (3) in the main text, the total propagator in the basis $\{|g\rangle, |f\rangle, |e\rangle\}$ is given by

$$\begin{aligned} U^{(2)} &= U_2(A_2,\Theta_2,\phi_2,\varphi_2)U_1(A_1,\Theta_1,\phi_1,\varphi_1) \\ &= \begin{bmatrix} \cos^2\Theta_2+\sin^2\Theta_2\cos\frac{A_2}{2} & -e^{i\Psi_2}\sin^2\frac{A_2}{4}\sin 2\Theta_2 & -ie^{i\phi_2}\sin\Theta_2\sin\frac{A_2}{2} \\ -e^{-i\Psi_2}\sin^2\frac{A_2}{4}\sin 2\Theta_2 & \sin^2\Theta_2+\cos^2\Theta_2\cos\frac{A_2}{2} & -ie^{i\varphi_2}\cos\Theta_2\sin\frac{A_2}{2} \\ -ie^{-i\phi_2}\sin\Theta_2\sin\frac{A_2}{2} & -ie^{-i\varphi_2}\cos\Theta_2\sin\frac{A_2}{2} & \cos\frac{A_2}{2} \end{bmatrix} \\ &\times \begin{bmatrix} \cos^2\Theta_1+\sin^2\Theta_1\cos\frac{A_1}{2} & -e^{i\Psi_1}\sin^2\frac{A_1}{4}\sin 2\Theta_1 & -ie^{i\phi_1}\sin\Theta_1\sin\frac{A_1}{2} \\ -e^{-i\Psi_1}\sin^2\frac{A_1}{4}\sin 2\Theta_1 & \sin^2\Theta_1+\cos^2\Theta_1\cos\frac{A_1}{2} & -ie^{i\varphi_1}\cos\Theta_1\sin\frac{A_1}{2} \\ -ie^{-i\phi_1}\sin\Theta_1\sin\frac{A_1}{2} & -ie^{-i\varphi_1}\cos\Theta_1\sin\frac{A_1}{2} & \cos\frac{A_1}{2} \end{bmatrix} \\ &= \begin{bmatrix} U_{11}^{(2)} & U_{12}^{(2)} & U_{13}^{(2)} \\ U_{21}^{(2)} & U_{22}^{(2)} & U_{23}^{(2)} \\ U_{31}^{(2)} & U_{32}^{(2)} & U_{33}^{(2)} \end{bmatrix}. \end{aligned} \tag{B1}$$

When the system is in the ground state $|g\rangle$, the time evolution of the system state reads $|\psi(t)\rangle = U_{11}^{(2)}|g\rangle + U_{21}^{(2)}|f\rangle + U_{31}^{(2)}|e\rangle$. Consider the error ϵ occurring in the pulse area: $\tilde{A}_n = A_n(1+\epsilon)$, $n = 1, 2$. The transition amplitude of the state $|f\rangle$ can be rewritten as

$$\begin{aligned} U_{21}^{(2)}(\epsilon) = &-e^{-i\Psi_1}\sin^2\frac{\tilde{A}_1}{4}\sin 2\Theta_1(\sin^2\Theta_2 + \cos\frac{\tilde{A}_2}{2}\cos^2\Theta_2) - e^{-i\Psi_2}\sin^2\frac{\tilde{A}_2}{4}\sin 2\Theta_2(\cos^2\Theta_1 + \cos\frac{\tilde{A}_1}{2}\sin^2\Theta_1) \\ &-e^{-i(\phi_1-\varphi_2)}\sin\Theta_1\cos\Theta_2\sin\frac{\tilde{A}_1}{2}\sin\frac{\tilde{A}_2}{2}, \end{aligned} \tag{B2}$$

where $\Psi_n = \phi_n - \varphi_n$.

The transition probability of the state $|f\rangle$ is equal to the modular squaring of the probability amplitude, i.e., $|U_{21}^{(2)}|^2$. Hence, the transition probability carries the erroneous pulse area $\tilde{A}_n$ as

$$\begin{aligned} P_2(\epsilon) = &\sin^2\Theta_1\cos^2\Theta_2\sin^2\frac{\tilde{A}_1}{2}\sin^2\frac{\tilde{A}_2}{2} + 8\Big[\cos^2\Theta_2\sin\Theta_1\sin\Theta_2\sin^3\frac{\tilde{A}_2}{4}\sin\frac{\tilde{A}_1}{2}\cos\frac{\tilde{A}_2}{4}\cos(\phi_1-\phi_2)\cos2\Theta_1\sin^2\frac{\tilde{A}_1}{4} + \cos^2\frac{\tilde{A}_1}{4} \\ &+\sin^2\Theta_1\cos\Theta_1\cos\Theta_2\sin^3\frac{\tilde{A}_1}{4}\cos\frac{\tilde{A}_1}{4}\sin\frac{\tilde{A}_2}{2}\cos(\varphi_1-\varphi_2)\cos^2\Theta_2\cos\frac{\tilde{A}_2}{2} + \sin^2\Theta_2\Big] \\ &+\sin^2 2\Theta_1\sin^4\frac{\tilde{A}_1}{4}\Big[\cos^2\Theta_2\cos\frac{\tilde{A}_2}{2} + \sin^2\Theta_2\Big]^2 + \sin^2 2\Theta_2\sin^4\frac{\tilde{A}_2}{4}\Big[\sin^2\Theta_1\cos\frac{\tilde{A}_1}{2} + \cos^2\Theta_1\Big]^2 \\ &+2\sin 2\Theta_1\sin 2\Theta_2\sin^2\frac{\tilde{A}_1}{4}\sin^2\frac{\tilde{A}_2}{4}\Big[\cos 2\Theta_1\sin^2\frac{\tilde{A}_1}{4} + \cos^2\frac{\tilde{A}_1}{4}\Big]\Big[\cos^2\Theta_2\cos\frac{\tilde{A}_2}{2} + \sin^2\Theta_2\Big]\cos\Gamma_1, \end{aligned} \tag{B3}$$

where $\Gamma_1 = \Psi_1 - \Psi_2$. After substituting the pulse area $A_1 = A_2 = 2\pi$ into Eq. (B3), we have

$$\begin{aligned} P_2(\epsilon) = &\sin^2\Theta_1\cos^2\Theta_2\sin^4\pi\epsilon + \cos^4\frac{\pi\epsilon}{2}\big[\sin^2 2\Theta_1(\sin^2\Theta_2 - \cos^2\Theta_2\cos\pi\epsilon)^2 + \sin^2 2\Theta_2(\cos^2\Theta_1 - \sin^2\Theta_1\cos\pi\epsilon)^2\big] \\ &+2\sin 2\Theta_1\sin 2\Theta_2\cos^4\frac{\pi\epsilon}{2}(\cos 2\Theta_1\cos^2\frac{\pi\epsilon}{2} + \sin^2\frac{\pi\epsilon}{2})(\sin^2\Theta_2 - \cos^2\Theta_2\cos\pi\epsilon)\cos\Gamma_1 \\ &+4\sin^2\pi\epsilon\cos^2\frac{\pi\epsilon}{2}\big[\sin\Theta_1\sin\Theta_2\cos^2\Theta_2\cos(\phi_1-\phi_2)(\cos 2\Theta_1\cos^2\frac{\pi\epsilon}{2} + \sin^2\frac{\pi\epsilon}{2}) \\ &+\cos\Theta_1\cos\Theta_2\sin^2\Theta_1\cos(\varphi_1-\varphi_2)(\sin^2\Theta_2 - \cos^2\Theta_2\cos\pi\epsilon)\big]. \end{aligned} \tag{B4}$$

Then, by the Taylor expansion, $P_2(\epsilon)$ could be written as the following form (up to the second-order term):

$$P_2(\epsilon) = \alpha_{2,0} + \alpha_{2,2}\epsilon^2 + O(\epsilon^4). \tag{B5}$$

Here, the zero-order is the precise transition probability, and the goal of designing the composite pulses sequence is to eliminate as many of the high-order coefficients as possible. Note that all odd-order coefficients are eliminated due to the choice of $A_1 = A_2 = 2\pi$. The expressions of the zeroth-order and the second-order coefficients are

$$\alpha_{2,0} = \frac{1}{2}\big(1 - \cos 4\Theta_1\cos 4\Theta_2 - \cos\Gamma_1\sin 4\Theta_1\sin 4\Theta_2\big), \tag{B6}$$

$$\begin{aligned} \alpha_{2,2} = &\frac{\pi^2}{4}\big[\sin4\Theta_1(\sin2\Theta_2 + 2\sin4\Theta_2) - \sin2\Theta_1\sin4\Theta_2\big]\cos\Gamma_1 + \frac{\pi^2}{2}(\cos4\Theta_1\cos4\Theta_2 - \sin^2 2\Theta_1\cos2\Theta_2 + \cos2\Theta_1\sin^2 2\Theta_2 - 1) \\ &+2\pi^2\big[\sin\Theta_2\cos^2\Theta_2(\sin 3\Theta_1 - \sin\Theta_1)\cos(\phi_1-\phi_2) - \sin^2\Theta_1\cos\Theta_1(\cos\Theta_2 + \cos 3\Theta_2)\cos(\varphi_1-\varphi_2)\big] \end{aligned} \tag{B7}$$

In the two-pulses sequence, there are only two parameters, Θ_1 and Θ_2. So, only two equations can be satisfied, i.e.,

$$\begin{cases} \alpha_{2,0} = 1, & \text{(B8)} \\ \alpha_{2,2} = 0. & \text{(B9)} \end{cases}$$

Note that the expression given by Eq. (B6) can be rearranged by $\alpha_{2,0} = 1/2\big[1 - \mathcal{A}\cos(4\Theta_1 - \beta)\big]$, where $\mathcal{A} = \sqrt{\cos^2 4\Theta_2 + \cos^2\Gamma_1\sin^2 4\Theta_2}$. Remarkably, the following inequality is always satisfied:

$$\mathcal{A} = \sqrt{\cos^2 4\Theta_2 + \cos^2\Gamma_1\sin^2 4\Theta_2} \le \sqrt{\cos^2 4\Theta_2 + \sin^2 4\Theta_2} = 1. \tag{B10}$$

Only when $\Gamma_1 = m\pi$ could there be an equality, where m is an arbitrary integer. In other words, the equation $\alpha_{2,0} = 1$ has real solutions if and only if $\Gamma_1 = m\pi$. For simplicity, we set $\Gamma_1 = 0$ in the main text, and Eqs. (B8) and (B9) become

$$\begin{cases} \sin^2 2(\Theta_1 - \Theta_2) = 1, & \text{(B11)} \\ \pi^2\sin 2(\Theta_2 - \Theta_1)\Big[\sin 2(\Theta_1 - \Theta_2) + \cos\Theta_2(2\sin\Theta_1 + \sin\Theta_2) + \sin\Theta_1\cos\Theta_1\Big] = 0. & \text{(B12)} \end{cases}$$

One solution of Eqs. (B11) and (B12) can be written as

$$\Theta_1 = m\pi + \frac{\pi}{8},\ \Theta_2 = m\pi + \frac{3\pi}{8}, \tag{B13}$$

where m is an arbitrary integer. With this group of solutions, the final propagator without errors becomes (in the basis $\{|g\rangle, |f\rangle, |e\rangle\}$)

$$U^{(2)} = i \begin{bmatrix} 0 & 1 & 0 \\ 1 & 0 & 0 \\ 0 & 0 & -i \end{bmatrix}. \tag{B14}$$

This propagator is recognized as an X gate with the global phase factor i. For the initial state of the system $|\psi_i\rangle = |g\rangle$, the final state would become $|\psi_f\rangle = i|f\rangle$. Similarly, when the phase difference $\Psi = 0$, by this group of solutions, we could also obtain a Y gate,

$$U^{(2)} = i \begin{bmatrix} 0 & -i & 0 \\ i & 0 & 0 \\ 0 & 0 & -i \end{bmatrix} \tag{B15}$$

with the same global phase factor. For the initial state of the system $|\psi_i\rangle = |g\rangle$, the final state would become $|\psi_f\rangle = -|f\rangle$. Note that both the X gate and the Y gate could achieve the population inversion, and the phase $\pi/2$ (π) of the final state for $\Psi = \pi/2$ ($\Psi = 0$) is the global phase, which can be ignored. As a result, the transition probability of the state $|f\rangle$ is only associated with its amplitude, and the Taylor series is

$$P_2(\epsilon) = 1 + O(\epsilon^4),$$

which is accurate to the fourth order in the pulse area error ϵ.

[1] J. L. Krause, D. H. Reitze, G. D. Sanders, A. V. Kuznetsov, and C. J. Stanton, Quantum control in quantum wells, Phys. Rev. B **57**, 9024 (1998).

[2] V. Ramakrishna, K. L. Flores, H. Rabitz, and R. J. Ober, Quantum control by decompositions of SU(2), Phys. Rev. A **62**, 053409 (2000).

[3] R. Vilela Mendes and V. I. Man'ko, Quantum control and the Strocchi map, Phys. Rev. A **67**, 053404 (2003).

[4] A. M. Brańczyk, P. E. M. F. Mendonça, A. Gilchrist, A. C. Doherty, and S. D. Bartlett, Quantum control of a single qubit, Phys. Rev. A **75**, 012329 (2007).

[5] R. Wang and Y.-Y. Niu, Quantum control of the dissociation of LiH molecules with two intense laser pulses, Phys. Rev. A **102**, 013113 (2020).

[6] R. Zhang, Y.-F. Liu, and T. Chen, Non-Hermiticity-induced quantum control of localization in quantum walks, Phys. Rev. A **102**, 022218 (2020).

[7] M. Dalgaard, F. Motzoi, J. H. M. Jensen, and J. Sherson, Hessian-based optimization of constrained quantum control, Phys. Rev. A **102**, 042612 (2020).

[8] T. Chen and Z.-Y. Xue, High-Fidelity and Robust Geometric Quantum Gates that Outperform Dynamical Ones, Phys. Rev. Appl. **14**, 064009 (2020).

[9] M. A. Nielsen and I. L. Chuang, *Quantum Computation and Quantum Information* (Cambridge University Press, Cambridge, 2000).

[10] C. Avinadav, R. Fischer, P. London, and D. Gershoni, Time-optimal universal control of two-level systems under strong driving, Phys. Rev. B **89**, 245311 (2014).

[11] K. Børkje, A. Nunnenkamp, J. D. Teufel, and S. M. Girvin, Signatures of Nonlinear Cavity Optomechanics in the Weak Coupling Regime, Phys. Rev. Lett. **111**, 053603 (2013).

[12] P. Doria, T. Calarco, and S. Montangero, Optimal Control Technique for Many-Body Quantum Dynamics, Phys. Rev. Lett. **106**, 190501 (2011).

[13] T. Caneva, T. Calarco, and S. Montangero, Chopped random-basis quantum optimization, Phys. Rev. A **84**, 022326 (2011).

[14] A. Baksic, H. Ribeiro, and A. A. Clerk, Speeding up Adiabatic Quantum State Transfer by Using Dressed States, Phys. Rev. Lett. **116**, 230503 (2016).

[15] X. Wang, M. Allegra, K. Jacobs, S. Lloyd, C. Lupo, and M. Mohseni, Quantum Brachistochrone Curves as Geodesics: Obtaining Accurate Minimum-Time Protocols for the Control of Quantum Systems, Phys. Rev. Lett. **114**, 170501 (2015).

[16] S. Bao, S. Kleer, R. Wang, and A. Rahmani, Optimal control of superconducting gmon qubits using Pontryagin's minimum principle: Preparing a maximally entangled state with singular bang-bang protocols, Phys. Rev. A **97**, 062343 (2018).

[17] Y.-H. Chen, Z.-C. Shi, J. Song, Y. Xia, and S.-B. Zheng, Optimal shortcut approach based on an easily obtained intermediate Hamiltonian, Phys. Rev. A **95**, 062319 (2017).

[18] N. Leung, M. Abdelhafez, J. Koch, and D. Schuster, Speedup for quantum optimal control from automatic differentiation based on graphics processing units, Phys. Rev. A **95**, 042318 (2017).

[19] R.-B. Wu, B. Chu, D. H. Owens, and H. Rabitz, Data-driven gradient algorithm for high-precision quantum control, Phys. Rev. A **97**, 042122 (2018).

[20] F.-Y. Zhang and C.-P. Yang, Generation of generalized hybrid entanglement in cavity electro–optic systems, Quantum Sci. Technol. **6**, 025003 (2021).

[21] Q. Lin and J. Li, Quantum control gates with weak cross-Kerr nonlinearity, Phys. Rev. A **79**, 022301 (2009).

[22] R. Wu, R. Chakrabarti, and H. Rabitz, Optimal control theory for continuous-variable quantum gates, Phys. Rev. A **77**, 052303 (2008).

[23] Y.-H. Kang, Y.-H. Chen, Z.-C. Shi, B.-H. Huang, J. Song, and Y. Xia, Nonadiabatic holonomic quantum computation using Rydberg blockade, Phys. Rev. A **97**, 042336 (2018).

[24] R. L. Kosut, M. D. Grace, and C. Brif, Robust control of quantum gates via sequential convex programming, Phys. Rev. A **88**, 052326 (2013).

[25] S. S. Hegde, J. Zhang, and D. Suter, Efficient Quantum Gates for Individual Nuclear Spin Qubits by Indirect Control, Phys. Rev. Lett. **124**, 220501 (2020).

[26] X. Wu, S. L. Tomarken, N. A. Petersson, L. A. Martinez, Y. J. Rosen, and J. L. DuBois, High-Fidelity Software-Defined Quantum Logic on a Superconducting Qudit, Phys. Rev. Lett. **125**, 170502 (2020).

[27] C.-Y. Guo, L.-L. Yan, S. Zhang, S.-L. Su, and W. Li, Optimized geometric quantum computation with a mesoscopic ensemble of Rydberg atoms, Phys. Rev. A **102**, 042607 (2020).

[28] G. Dridi, K. Liu, and S. Guérin, Optimal Robust Quantum Control by Inverse Geometric Optimization, Phys. Rev. Lett. **125**, 250403 (2020).

[29] Y.-H. Kang, Z.-C. Shi, B.-H. Huang, J. Song, and Y. Xia, Flexible scheme for the implementation of nonadiabatic geometric quantum computation, Phys. Rev. A **101**, 032322 (2020).

[30] T. Chen, P. Shen, and Z.-Y. Xue, Robust and Fast Holonomic Quantum Gates with Encoding on Superconducting Circuits, Phys. Rev. Appl. **14**, 034038 (2020).

[31] C. Zhang, T. Chen, S. Li, X. Wang, and Z.-Y. Xue, High-fidelity geometric gate for silicon-based spin qubits, Phys. Rev. A **101**, 052302 (2020).

[32] Z.-Y. Xue, J. Zhou, Y.-M. Chu, and Y. Hu, Nonadiabatic holonomic quantum computation with all-resonant control, Phys. Rev. A **94**, 022331 (2016).

[33] X. Ge, H. Ding, H. Rabitz, and R.-B. Wu, Robust quantum control in games: An adversarial learning approach, Phys. Rev. A **101**, 052317 (2020).

[34] Y. Zhong and J. Jing, Enhancement of tripartite quantum correlation by coherent feedback control, Phys. Rev. A **101**, 023813 (2020).

[35] A. Ma, A. B. Magann, T.-S. Ho, and H. Rabitz, Optimal control of coupled quantum systems based on the first-order Magnus expansion: Application to multiple dipole-dipole-coupled molecular rotors, Phys. Rev. A **102**, 013115 (2020).

[36] K. Takeda, A. Noiri, J. Yoneda, T. Nakajima, and S. Tarucha, Resonantly Driven Singlet-Triplet Spin Qubit in Silicon, Phys. Rev. Lett. **124**, 117701 (2020).

[37] M. L. Goldman, T. L. Patti, D. Levonian, S. F. Yelin, and M. D. Lukin, Optical Control of a Single Nuclear Spin in the Solid State, Phys. Rev. Lett. **124**, 153203 (2020).

[38] D. Hayes, D. Stack, B. Bjork, A. C. Potter, C. H. Baldwin, and R. P. Stutz, Eliminating Leakage Errors in Hyperfine Qubits, Phys. Rev. Lett. **124**, 170501 (2020).

[39] L. Allen and J. H. Eberly, *Optical resonance and two-level atoms* (Dover Publications, New York, 1987).

[40] J. S. Melinger, S. R. Gandhi, A. Hariharan, J. X. Tull, and W. S. Warren, Generation of narrowband inversion with broadband laser pulses, Phys. Rev. Lett. **68**, 2000 (1992).

[41] J. S. Melinger, S. R. Gandhi, A. Hariharan, D. Goswami, and W. S. Warren, Adiabatic population transfer with frequency-swept laser pulses, J. Chem. Phys. **101**, 6439 (1994).

[42] I. R. Solá, V. S. Malinovsky, B. Y. Chang, J. Santamaria, and K. Bergmann, Coherent population transfer in three-level Λ systems by chirped laser pulses: Minimization of the intermediate-level population, Phys. Rev. A **59**, 4494 (1999).

[43] Y. B. Band and O. Magnes, Chirped adiabatic passage with temporally delayed pulses, Phys. Rev. A **50**, 584 (1994).

[44] N. Vitanov, T. Halfmann, B. Shore, and K. Bergmann, Laser-induced population transfer by adiabatic passage techniques, Annu. rev. Phys. Chem. **52**, 763 (2001).

[45] D. Goswami, Optical pulse shaping approaches to coherent control, Phys. Rep. **374**, 385 (2003).

[46] U. Gaubatz, P. Rudecki, S. Schiemann, and K. Bergmann, Population transfer between molecular vibrational levels by stimulated Raman scattering with partially overlapping laser fields. A new concept and experimental results, J. Chem. Phys. **92**, 5363 (1990).

[47] P. Marte, P. Zoller, and J. L. Hall, Coherent atomic mirrors and beam splitters by adiabatic passage in multilevel systems, Phys. Rev. A **44**, R4118 (1991).

[48] B. W. Shore, K. Bergmann, A. Kuhn, S. Schiemann, J. Oreg, and J. H. Eberly, Laser-induced population transfer in multistate systems: A comparative study, Phys. Rev. A **45**, 5297 (1992).

[49] N. V. Vitanov, A. A. Rangelov, B. W. Shore, and K. Bergmann, Stimulated Raman adiabatic passage in physics, chemistry, and beyond, Rev. Mod. Phys. **89**, 015006 (2017).

[50] D. Guéry-Odelin, A. Ruschhaupt, A. Kiely, E. Torrontegui, S. Martínez-Garaot, and J. G. Muga, Shortcuts to adiabaticity: Concepts, methods, and applications, Rev. Mod. Phys. **91**, 045001 (2019).

[51] X. Chen, E. Torrontegui, and J. G. Muga, Lewis-Riesenfeld invariants and transitionless quantum driving, Phys. Rev. A **83**, 062116 (2011).

[52] X. Chen, I. Lizuain, A. Ruschhaupt, D. Guéry-Odelin, and J. G. Muga, Shortcut to Adiabatic Passage in Two- and Three-Level Atoms, Phys. Rev. Lett. **105**, 123003 (2010).

[53] H. R. Lewis and W. B. Riesenfeld, An Exact Quantum Theory of the Time-Dependent Harmonic Oscillator and of a Charged Particle in a Time-Dependent Electromagnetic Field, J. Math. Phys. **10**, 1458 (1969).

[54] M. Demirplak and S. A. Rice, Adiabatic Population Transfer with Control Fields, J. Phys. Chem. A **107**,

9937 (2003).
[55] M. Demirplak and S. A. Rice, Assisted Adiabatic Passage Revisited, J. Phys. Chem. B **109**, 6838 (2005).
[56] M. V. Berry, Transitionless quantum driving, J. Phys. A **42**, 365303 (2009).
[57] C. Lin, D. Sels, and Y. Wang, Time-optimal control of a dissipative qubit, Phys. Rev. A **101**, 022320 (2020).
[58] E. T. Holland, K. A. Wendt, K. Kravvaris, X. Wu, W. E. Ormand, J. L. DuBois, S. Quaglioni, and F. Pederiva, Optimal control for the quantum simulation of nuclear dynamics, Phys. Rev. A **101**, 062307 (2020).
[59] C. Lin, D. Sels, Y. Ma, and Y. Wang, Stochastic optimal control formalism for an open quantum system, Phys. Rev. A **102**, 052605 (2020).
[60] M. Larocca, E. Calzetta, and D. A. Wisniacki, Exploiting landscape geometry to enhance quantum optimal control, Phys. Rev. A **101**, 023410 (2020).
[61] J. Tian, H. Liu, Y. Liu, P. Yang, R. Betzholz, R. S. Said, F. Jelezko, and J. Cai, Quantum optimal control using phase-modulated driving fields, Phys. Rev. A **102**, 043707 (2020).
[62] Z. An, H.-J. Song, Q.-K. He, and D. L. Zhou, Quantum optimal control of multilevel dissipative quantum systems with reinforcement learning, Phys. Rev. A **103**, 012404 (2021).
[63] J. H. Plantenberg, P. C. de Groot, C. J. P. M. Harmans, and J. E. Mooij, Demonstration of controlled-NOT quantum gates on a pair of superconducting quantum bits, Nature **447**, 836 (2007).
[64] S. J. Glaser, U. Boscain, T. Calarco, C. P. Koch, W. Köckenberger, R. Kosloff, I. Kuprov, B. Luy, S. Schirmer, T. Schulte-Herbrüggen, D. Sugny, and F. K. Wilhelm, Training Schrödinger's cat: Quantum optimal control, Eur. Phys. J. D **69** (2015).
[65] S. Wimperis, Broadband, Narrowband, and Passband Composite Pulses for Use in Advanced NMR Experiments, J. Magn. Reson. **109**, 221 (1994).
[66] M. H. Levitt, Composite pulses, Prog. NMR Spectrosc. **18**, 61 (1986).
[67] S. Wimperis, Iterative schemes for phase-distortionless composite 180° pulses, J. Magn. Reson. **93**, 199 (1991).
[68] S. Husain, M. Kawamura, and J. A. Jones, Further analysis of some symmetric and antisymmetric composite pulses for tackling pulse strength errors, J. Magn. Reson. **230**, 145 (2013).
[69] G. T. Genov, D. Schraft, T. Halfmann, and N. V. Vitanov, Correction of Arbitrary Field Errors in Population Inversion of Quantum Systems by Universal Composite Pulses, Phys. Rev. Lett. **113**, 043001 (2014).
[70] S. S. Ivanov and N. V. Vitanov, High-fidelity local addressing of trapped ions and atoms by composite sequences of laser pulses, Opt. Lett. **36**, 1275 (2011).
[71] B. T. Torosov and N. V. Vitanov, Arbitrarily accurate variable rotations on the Bloch sphere by composite pulse sequences, Phys. Rev. A **99**, 013402 (2019).
[72] B. T. Torosov and N. V. Vitanov, Smooth composite pulses for high-fidelity quantum information processing, Phys. Rev. A **83**, 053420 (2011).
[73] J. A. Jones, Designing short robust NOT gates for quantum computation, Phys. Rev. A **87**, 052317 (2013).
[74] G. T. Genov, M. Hain, N. V. Vitanov, and T. Halfmann, Universal composite pulses for efficient population inversion with an arbitrary excitation profile, Phys. Rev. A **101**, 013827 (2020).
[75] G. Dridi, M. Mejatty, S. J. Glaser, and D. Sugny, Robust control of a not gate by composite pulses, Phys. Rev. A **101**, 012321 (2020).
[76] B. T. Torosov, B. W. Shore, and N. V. Vitanov, Coherent control techniques for two-state quantum systems: A comparative study, Phys. Rev. A **103**, 033110 (2021).
[77] B. T. Torosov, S. S. Ivanov, and N. V. Vitanov, Narrowband and passband composite pulses for variable rotations, Phys. Rev. A **102**, 013105 (2020).
[78] E. Kyoseva, H. Greener, and H. Suchowski, Detuning-modulated composite pulses for high-fidelity robust quantum control, Phys. Rev. A **100**, 032333 (2019).
[79] X. Wang, L. S. Bishop, J. Kestner, E. Barnes, K. Sun, and S. D. Sarma, Composite pulses for robust universal control of singlet–triplet qubits, Nat. Commun. **3** (2012).
[80] X. Wang, L. S. Bishop, E. Barnes, J. P. Kestner, and S. D. Sarma, Robust quantum gates for singlet-triplet spin qubits using composite pulses, Phys. Rev. A **89**, 022310 (2014).
[81] B. T. Torosov and N. V. Vitanov, High-fidelity composite quantum gates for Raman qubits, Phys. Rev. Research **2**, 043194 (2020).
[82] Z.-C. Shi, H.-N. Wu, L.-T. Shen, J. Song, Y. Xia, X. X. Yi, and S.-B. Zheng, Robust single-qubit gates by composite pulses in three-level systems, Phys. Rev. A **103**, 052612 (2021).
[83] B. T. Torosov, M. Drewsen, and N. V. Vitanov, Chiral resolution by composite Raman pulses, Phys. Rev. Research **2**, 043235 (2020).
[84] N. Mansourzadeh-Ashkani, M. Saadati-Niari, F. Zolfagharpour, and B. Nedaee-Shakarab, Nuclear-state population transfer using composite stimulated Raman adiabatic passage, Nucl. Phys. A **1007**, 122119 (2021).
[85] J. Ghosh, S. N. Coppersmith, and M. Friesen, Pulse sequences for suppressing leakage in single-qubit gate operations, Phys. Rev. B **95**, 241307 (2017).
[86] M. Friesen, J. Ghosh, M. A. Eriksson, and S. N. Coppersmith, A decoherence-free subspace in a charge quadrupole qubit, Nat. Commun. **8**, 15923 (2017).
[87] Z.-C. Shi, C. Zhang, D. Ran, Y. Xia, R. Ianconescu, A. Friedman, X. X. Yi, and S.-B. Zheng, Composite pulses for high fidelity population transfer in three-level systems, New J. Phys. **24**, 023014 (2022).
[88] P. Pillet, C. Valentin, R.-L. Yuan, and J. Yu, Adiabatic population transfer in a multilevel system, Phys. Rev. A **48**, 845 (1993).
[89] P. D. Featonby, G. S. Summy, J. L. Martin, H. Wu, K. P. Zetie, C. J. Foot, and K. Burnett, Adiabatic transfer for atomic interferometry, Phys. Rev. A **53**, 373 (1996).
[90] P. Král and M. Shapiro, Cyclic Population Transfer in Quantum Systems with Broken Symmetry, Phys. Rev. Lett. **87**, 183002 (2001).
[91] X. Lacour, N. Sangouard, S. Guérin, and H. R. Jauslin, Arbitrary state controlled-unitary gate by adiabatic passage, Phys. Rev. A **73**, 042321 (2006).
[92] J. Klein, F. Beil, and T. Halfmann, Robust Population Transfer by Stimulated Raman Adiabatic Passage in a Pr^{3+}:Y_2SiO_5 Crystal, Phys. Rev. Lett. **99**, 113003 (2007).
[93] J. Klein, F. Beil, and T. Halfmann, Experimental investigations of stimulated Raman adiabatic passage

in a doped solid, Phys. Rev. A **78**, 033416 (2008).
[94] S. Longhi, Quantum-optical analogies using photonic structures, Laser Photonics Rev. **3**, 243 (2009).
[95] Y.-D. Wang and A. A. Clerk, Using dark modes for high-fidelity optomechanical quantum state transfer, New J. Phys. **14**, 105010 (2012).
[96] M. O. Scully and M. S. Zubairy, *Quantum Optics* (Cambridge University Press, Cambridge, 1997).
[97] E. Brion, L. H. Pedersen, and K. Mølmer, Adiabatic elimination in a lambda system, J. Phys. A: Math. Theor. **40**, 1033 (2007).
[98] S. Shevchenko, S. Ashhab, and F. Nori, Landau-Zener-Stückelberg interferometry, Phys. Rep. **492**, 1 (2010).
[99] A. Politi, M. J. Cryan, J. G. Rarity, S. Yu, and J. L. O'Brien, Silica-on-Silicon Waveguide Quantum Circuits, Science **320**, 646 (2008).
[100] M. D. Reed, B. M. Maune, R. W. Andrews, M. G. Borselli, K. Eng, M. P. Jura, A. A. Kiselev, T. D. Ladd, S. T. Merkel, I. Milosavljevic, E. J. Pritchett, M. T. Rakher, R. S. Ross, A. E. Schmitz, A. Smith, J. A. Wright, M. F. Gyure, and A. T. Hunter, Reduced Sensitivity to Charge Noise in Semiconductor Spin Qubits via Symmetric Operation, Phys. Rev. Lett. **116**, 110402 (2016).
[101] Z.-L. Xiang, S. Ashhab, J. Q. You, and F. Nori, Hybrid quantum circuits: Superconducting circuits interacting with other quantum systems, Rev. Mod. Phys. **85**, 623 (2013).
[102] L.-X. Xia and Q.-T. Xie, Unconventional geometric quantum phase gates with two SQUIDs in a cavity, Opt. Commun. **281**, 2700 (2008).
[103] C.-P. Yang, S.-I. Chu, and S. Han, Possible realization of entanglement, logical gates, and quantum-information transfer with superconducting-quantum-interference-device qubits in cavity QED, Phys. Rev. A **67**, 042311 (2003).
[104] C.-P. Yang, S.-I. Chu, and S. Han, Quantum Information Transfer and Entanglement with SQUID Qubits in Cavity QED: A Dark-State Scheme with Tolerance for Nonuniform Device Parameter, Phys. Rev. Lett. **92**, 117902 (2004).
[105] Y.-H. Kang, Y.-H. Chen, Z.-C. Shi, J. Song, and Y. Xia, Fast preparation of W states with superconducting quantum interference devices by using dressed states, Phys. Rev. A **94**, 052311 (2016).
[106] C. Guarcello, R. Citro, O. Durante, F. S. Bergeret, A. Iorio, C. Sanz-Fernández, E. Strambini, F. Giazotto, and A. Braggio, rf-SQUID measurements of anomalous Josephson effect, Phys. Rev. Research **2**, 023165 (2020).
[107] J. Braumüller, L. Ding, A. P. Vepsäläinen, Y. Sung, M. Kjaergaard, T. Menke, R. Winik, D. Kim, B. M. Niedzielski, A. Melville, J. L. Yoder, C. F. Hirjibehedin, T. P. Orlando, S. Gustavsson, and W. D. Oliver, Characterizing and Optimizing Qubit Coherence Based on SQUID Geometry, Phys. Rev. Appl. **13**, 054079 (2020).
[108] M. Stern, G. Catelani, Y. Kubo, C. Grezes, A. Bienfait, D. Vion, D. Esteve, and P. Bertet, Flux Qubits with Long Coherence Times for Hybrid Quantum Circuits, Phys. Rev. Lett. **113**, 123601 (2014).
[109] P. J. Leek, M. Baur, J. M. Fink, R. Bianchetti, L. Steffen, S. Filipp, and A. Wallraff, Cavity Quantum Electrodynamics with Separate Photon Storage and Qubit Readout Modes, Phys. Rev. Lett. **104**, 100504 (2010).
[110] F. Yan, S. Gustavsson, A. Kamal, J. Birenbaum, A. P. Sears, D. Hover, T. J. Gudmundsen, D. Rosenberg, G. Samach, S. Weber, J. L. Yoder, T. P. Orlando, J. Clarke, A. J. Kerman, and W. D. Oliver, The flux qubit revisited to enhance coherence and reproducibility, Nat. Commun. **7**, 12964 (2016).
[111] Y. Ma, X. Pan, W. Cai, X. Mu, Y. Xu, L. Hu, W. Wang, H. Wang, Y. P. Song, Z.-B. Yang, S.-B. Zheng, and L. Sun, Manipulating Complex Hybrid Entanglement and Testing Multipartite Bell Inequalities in a Superconducting Circuit, Phys. Rev. Lett. **125**, 180503 (2020).
[112] Y. Xu, Y. Ma, W. Cai, X. Mu, W. Dai, W. Wang, L. Hu, X. Li, J. Han, H. Wang, Y. P. Song, Z.-B. Yang, S.-B. Zheng, and L. Sun, Demonstration of Controlled-Phase Gates between Two Error-Correctable Photonic Qubits, Phys. Rev. Lett. **124**, 120501 (2020).
[113] T. Niemczyk, F. Deppe, H. Huebl, E. P. Menzel, F. Hocke, M. J. Schwarz, J. J. Garcia-Ripoll, D. Zueco, T. Hümmer, E. Solano, A. Marx, and R. Gross, Circuit quantum electrodynamics in the ultrastrong-coupling regime, Nat. Phys. **6**, 772 (2010).